Position resolution with prototypes of ALICE Transition Radiation Detector

Diploma Thesis

by

Oliver Busch

Gesellschaft für Schwerionenforschung

Darmstadt

May 2002

Position resolution with prototypes of ALICE Transition Radiation Detector

In this work we investigate the track reconstruction capabilities of prototype drift chambers for the Transition Radiation Detector (TRD) of the ALICE experiment, which will be located at CERN LHC. The TRD will serve as a trigger on high p_t electrons by means of track reconstruction in a magnetic field. The trigger capabilities of the detector will also provide the opportunity to select jet events.

In beam experiments at the secondary pion beam faciltity at GSI SIS we tested prototype drift chambers with pad readout, operated with a Xe,CO_2(15%) gas mixture in a magnetic field up to 0.3 T. We demonstrate the equivalence of different pad shapes, rectangular and chevron type pads, in terms of point resolution and track reconstruction. The influence of the signal-to-noise ratio and the angle of incidence of the primary particle is investigated. We study the effect of a deconvolution of the signal and demonstrate its benefit for the resolution of the detector. Under the operational conditions anticipated for ALICE, a point resolution better than 300 μm and an angular resolution better than 1° is achieved.

As an important application, the Lorentz angle of ionization electrons drifting in the TRD gas mixture has been measured directly for the first time. Our results agree with GARFIELD calculations.

We present Lorentz angle measurements in a Ne,CO_2(13%) mixture performed at the pion beam facility at CERN PS. The experimental results are in agreement with the calculations.

Ortsauflösung der Prototypen
für den ALICE Übergangsstrahlungsdetektor

In der vorliegenden Arbeit werden Driftkammerprototypen für den Übergangsstrahlungsdetektor (TRD) des ALICE Experiments am CERN LHC auf ihre Ortsauflösung untersucht. Die Spurrekonstruktion durch den TRD im Feld des L3 Magneten eröffnet die Möglichkeit, Teilchen mit hohem Transversalimpuls p_t zu identifizieren und somit Elektronen aus leptonischen Zerfällen schwerer Quarkonia sowie hadronische Jets zu selektieren.

Die Tests der Xe,CO_2-gefüllten Driftkammern wurden am sekundären Pionenstrahl des GSI SIS in Magnetfeldern bis zu 0.3 T durchgeführt. Wir vergleichen verschieden geformte Kathodenpads, Rechtecke und Chevrons, und demonstrieren deren Gleichwertigkeit für die Spurrekonstruktion. Der Einfluß des Signal/Rausch-Verhältnisses sowie des Einfallswinkels des primären Teilchens auf die Orts- und Winkelauflösung des Detektors wird untersucht. Wir zeigen, daß sich durch Dekonvolution des Detektorsignals eine Verbesserung der Auflösung erzielen läßt. Unsere Ergebnisse lassen für den TRD in ALICE eine Ortsauflösung besser als 300 μm und eine Winkelauflösung von weniger als 1° erwarten.

Die Messungen erlauben die direkte Bestimmung des Lorentzwinkels der TRD Gasmischung Xe,CO_2(15%). Diese Größe stellt eine wichtige Information für den TRD Trigger dar und wurde bisher noch nicht experimentell ermittelt. Unsere Ergebnisse stimmen mit Vorhersagen der GARFIELD Software überein.

Wir präsentieren Messungen des Lorentzwinkels in Ne,CO_2(13%), die am CERN PS durchgeführt wurden. Die experimentellen Ergebnisse und die Berechnungen durch GARFIELD stimmen überein.

Contents

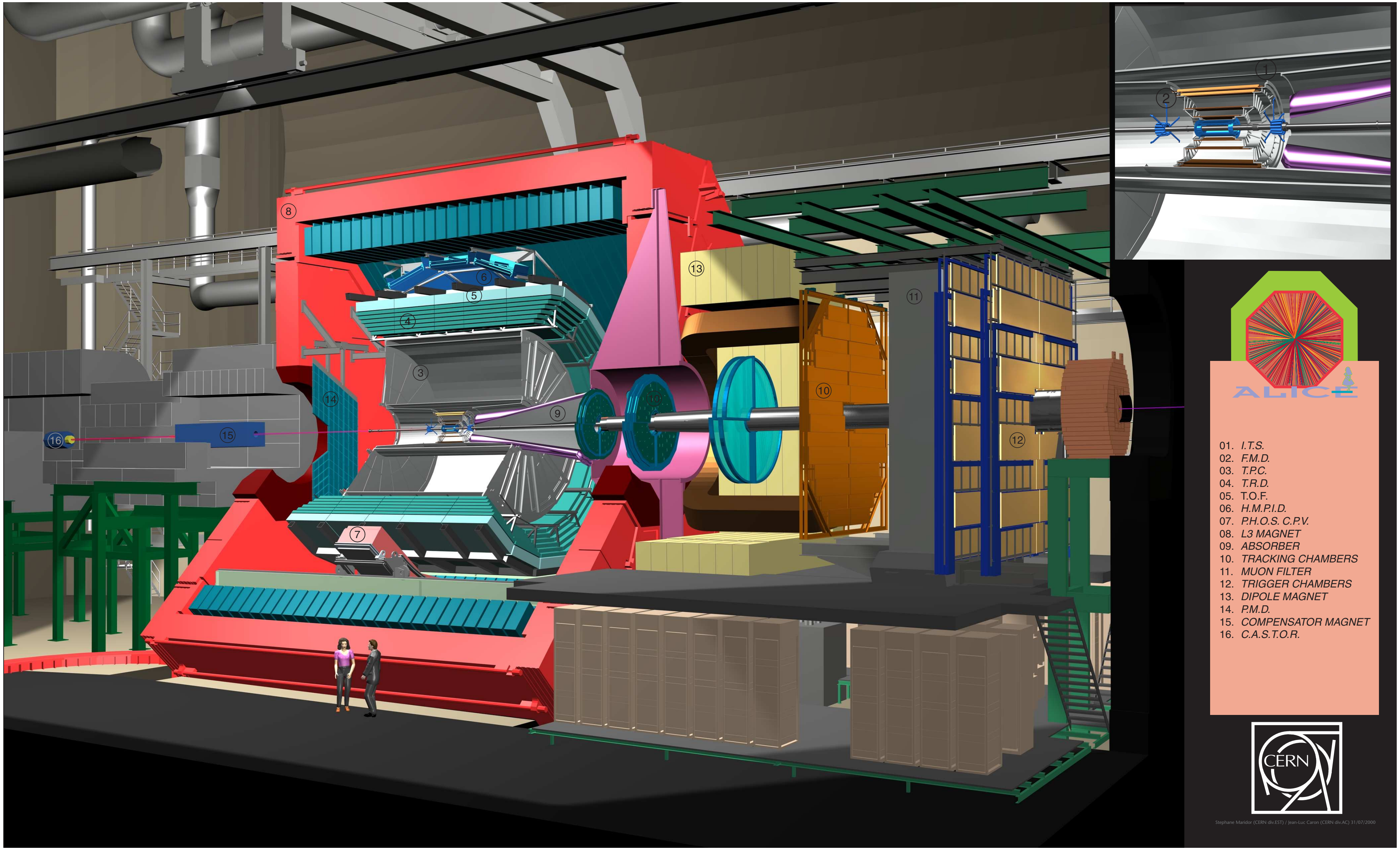

Figure 1.1: Layout of the ALICE experiment. The TRD is placed between TPC(3) and TOF(5).

1 Introduction: ALICE TRD

1.1 Physics motivation

By 2007, the Large Hadron Collider (LHC) at CERN will start operation. ALICE (A Large Ion Collider Experiment) [1] is a dedicated experiment to study heavy ion collisions, at a centre of mass energy up to 5.5 TeV per nucleon pair.

At such energies, the colliding nuclei interpenetrate each other. During their passage, multiple scattering among the quark and gluon constituents occurs, leading to a rapid generation of entropy and thereby to thermalisation. The separating nucleons leave behind a more or less equilibrated expanding medium, eventually decaying into hadrons. The energy deposited in the interaction zone is of the order of 1000 GeV/fm^3, the initial temperature about 1 GeV [2]. Under those extreme conditions, QCD, the gauge theory of the strong interaction, predicts the formation of a new state of matter, the Quark Gluon Plasma (QGP) [3]. Strongly interacting particles, normally confined into colour neutral hadrons, undergo a phase transition to a system of free quarks and gluons. Lattice QCD simulations predict a critical temperature of T=(175$\pm$10) MeV. After QGP formation in the early hot stage, the system in (local) thermal equilibrium expands and cools and undergoes the confining quark-hadron transition. The hadronic matter finally freezes out into the hadronic secondaries.

Apart from the vivid interest in the QCD phase diagram as a subject on its own, the QGP is important in a cosmological and astrophysical context. Up to $\sim$0.1 μs after the Big Bang, in the hot and dense early universe, the entire matter we observe today existed in the QGP phase. Today, conditions in the interior of neutron stars may be favorable for the persistence of the partonic phase.

How can we prove the formation of deconfined matter in the laboratory? The short life time of the fireball of the order of 10 fm/c rules out any direct observation of the QGP. We have to prove the existence and study the properties of the plasma by its effects on the remainders of the collision, the produced hadrons, electrons and photons. Physicists have to reconstruct the new state of matter from its ashes.

A wealth of ideas has been proposed, how this task could be accomplished. Ideally, the experiment has to show that some features of the data cannot be present without a QGP. ALICE, as the only dedicated heavy ion experiment at the LHC, is designed to measure a large set of observables over a maximum of achievable phase space.

1.2 The ALICE detector

The ALICE experimental setup is shown in Fig. 1.1. The experiment will have a central barrel, housed in the L3 magnet, covering the pseudorapidity range -0.9$\leq \eta \leq$0.9 (the pseudorapidity η is a measure of the the angle θ with respect to the beam axis, $\eta = -\ln(\tan\frac{\theta}{2})$), with complete azimuthal coverage. The central barrel comprises an inner tracking system of silicon detectors (ITS), a large time projecion chamber (TPC), a transition radiation detector (TRD) - prototypes for this detector are subject of this work - and a time-of-flight array (TOF). In addition, there will be at mid-rapidity ($\theta = 90°$) two single arm detectors, an array of ring-imaging Cherenkov counters (HMPID) to identify high-momentum hadrons and an array of crystals (PHOS) for the detection of photons. This central barrel will be complemented at pseudorapidities of η=2.5-4 by a muon spectrometer with its own dipole magnet. At more forward and backward rapidities detectors will be located to measure the multiplicity of charged particles and the time of an interaction, both also for trigger purposes, as well as several more specialized detectors.

1.3 ALICE TRD: implementation and performance

The TRD consists of 540 drift chambers, arranged in 6 radial layers around the beam axis (which is labelled z-axis in this work, using standard spherical coordinates) and in 18 azimuthal sectors in ϕ, covering the full azimuthal angle of 2π. Along z, 5 segments cover a total length of 7 m; the radial coverage is 2.9 m$\leq r \leq$3.7 m. The total volume of the TRD is $\sim$27 m^3; the largest drift chamber module has a surface of 1.2 $\times$ 1.6 m^2. The TRD has a radial thickness of X=14% X_0. In front of each chamber a radiator is attached. The radiators have a 'sandwich' structure: they consist of boxes of a Rohacell foam filled with polypropylene fibre mats.

An electron passing through the radiator emits transition radiation (TR) photons of an energy of typically 10 keV. Any highly relativistic charged particle traversing the boundary between two media of different dielectric constants produces TR. The phenomenon was first predicted by Ginzburg and Frank in 1946 [4]. The dependence of the TR yield on the Lorentz factor γ of the particle is used for particle identification: for electrons up to 2 GeV ($\gamma \approx$ 4000) a strong linear increase with the energy of the particle is observed, for higher Lorentz factors the yield approaches saturation. In a big momentum range, from 1-100 GeV/c, electrons are the only particles producing transition radiation. The TR photons are emitted at a small angle $\alpha \simeq 1/\gamma$ with respect to the trajectory of the incident particle. The sensitivity of the transition radiation process to the γ-factor of the particle is unique, any other process used for particle identification depends on β (e.g. Cherenkov radiation) or a combination of β and γ (e.g. the energy loss per unit track length dE/dx). To achieve a detectable yield of TR photons, a large number of boundaries has to be combined. For this purpose, stacks of hundreds of closely spaced foils have been constructed and used to study the characteristics of TR production. In ALICE TRD, polypropylene fibres and foams are adopted as radiator material, providing the necessary variations of the dielectrical constant by their microscopic structure. One radiator is attached to the entrance window of each drift chamber. Since the chambers are operated at overpressure, the radiator has to serve as mechanical support to the window. The design of the radiator is a compromise between TR yield and mechanical stability.

In addition to its electron-pion discrimination capabilities, the TRD is a powerful device to measure the trajectory of the incident particle. The track reconstruction performance of the TRD prototypes is subject of this work. Track reconstruction with the TRD will be used to trigger on high momentum particles. The detector operates in a magnetic field of B=0.4 T. The B-field lines are parallel to the beam axis. A charged particle in transverse motion experiences the Lorentz force and is deflected in ϕ direction. The drift chambers reconstruct the (r,ϕ) coordinate of the trajectory of an incident charged particle: the anode wires run in ϕ direction, 'spinning' around the beam axis, the longer edge of the pads is parallel to the beam axis. For given B, the curvature of the trajectory is inversely proportional to the particle's momentum. Selecting tracks with small deflection, the TRD allows to trigger on particles with a transverse momentum higher than 2-3 GeV/c.

To illustrate the role of the TRD for the ALICE physics performance, we present some examples out of the rich variety of proposed signatures for QGP formation. A probe to distinguish between confinement and deconfinement should ideally be present in the early stage of the collision and retain the information throughout the subsequent evolution. Quarkonia, as J/ψ and Υ, are such probes. The J/ψ meson is a bound state of a charm quark and antiquark ($c\bar{c}$) with a mass of ~3.1 GeV [5]. J/ψ is produced by gluon fusion in the early stage of the collision. In a QGP, bound partonic states cannot survive. The interaction of quarks in QCD is based on their intrinsic colour charge, and in a dense medium of free partons this charge is screened, in much the same way the electric charge which binds in a solid the electron to the nucleus is screened at high density, resulting in a phase transition from insulating to conducting matter (Debye effect) [6]. In QGP, the yield of J/ψ should therefore be suppressed (with respect to the yield in p-p collisions, appropriately scaled). One has to distinguish between effects of the partonic phase and absorption of preresonance states in cold matter, leading to 'normal' J/ψ suppression [7]. At CERN SPS, the J/ψ yield in Pb-Pb collisions at 158 GeV/c has been measured as function of centrality, and indeed 'anomalous' suppression beyond nuclear effects is observed and interpreted as signature of a discontinuity in the state of nuclear matter [8]. At LHC energies, however, statistical hadronization of directly produced charm could lead to an enhancement of the charmonium yield [9]. To determine possible thermal features of hadronization, it is desirable to measure not only charmonium yields but also the abundance of charmed mesons.

Mesons are detected via their leptonic (and semileptonic) decays. Electrons and muons are not subject to the strong interaction and leave the fireball unaffected by hadronic interactions. They retain the memory of the decay. Dileptons from quark-antiquark annihilation and thermal dileptons from the medium provide the most direct view of the reaction scenario. The electron identification capabilities offered by the TRD are essential to discriminate electrons against the large pionic background.

The TRD trigger on high momentum electrons increases statistics for the rare electromagnetic probes. It will provide the unique opportunity to measure, in the dielectron channel, the Υ meson family. The Υ is the beauty quark analogue to the J/ψ. Its yield should be affected by the QGP, in analogy to the charmonium. Due to its high mass, its production cross section is extremely small (in the order of 10 μb). Without a trigger, it could not be observed with sufficient statistics.

The trigger capability of the TRD also offers the interesting and unique possibility to trigger on jets, highly collimated sprays of hadrons. They can be selected requiring several (3 or more) high p_t tracks in one TRD module [2]. Jets are produced through hard scattering of partons in the very early stage of the collision. As the scattered quarks or gluons separate, the effective interaction between them increases. At some point, quarks and antiquarks are created, and the partons turn into colour neutral hadrons, the constituents of the jet. The initially scattered partons, leaving the interaction point, pass through the nuclear matter and the secondary medium produced by the collision. The effect of such a passage depends very strongly on the nature of this medium: the energy loss of partons in deconfined matter is much increased with respect to normal nuclear matter. The manifestation of the increased energy loss, jet quenching, is a remarkable signature of QGP formation, still under vivid theoretical investigation.

2 The experimental setup

In this chapter we explain the principles of particle detection and track reconstruction with the TRD drift chambers. We discuss the setup of the beam prototype tests and present measured pulse height distributions, which are closely related to the chamber geometry and are important for our method of position reconstruction.

2.1 Detector principle

The basic detecting element of the TRD is the drift chamber(DC). The chamber geometry is presented in Fig. 2.1 (left panel). The radiator shown in the figure is not to scale: with $\triangle$r$\approx$5 cm it is thicker than the chamber ($\triangle$r$=$3.7 cm). We distinguish between the drift region, defined as the space between the entrance window and the cathode wires, and the amplification region, between the cathode wires and the cathode pads. The field in the drift region is homogeneous. Its strength is governed by the negative voltage applied to the entrance window. The cathode wires and the cathode pad plane are grounded. In the present design [2], the operational drift voltage is -2.1 kV, the depth of the drift region ('drift length') 3.0 cm, resulting in a drift field of E=0.7 kV/cm. The depth of the amplification region, comprising the anode wires at positive voltage, is 0.7 cm. The chamber is filled with a gas mixture of Xe,CO_2(15%).

A particle traversing the chamber volume deposits part of its kinetic energy, ionizing the chamber gas. It leaves behind a trace of electron clusters along its track. In the homogeneous drift field, the electrons move towards the cathode wires at constant drift velocity. Arriving at the amplification region, the electrons move in the field of the anode wire. They are accelerated towards the wire and gain sufficient kinetic energy to ionize gas atoms, producing secondary ionization. A chain of such reactions leads to an avalanche of electrons and ions formed ('Townsend avalanche'), resulting in a significant amplification of the amount of charge created in the primary ionization, typically by a factor of 10^3. The electrons are absorbed by the anode wire. The positive ions from the avalanche move towards the cathode pads and wires. Due to their higher mass, they are much slower than the electrons. The ions induce the signal on the anode wire.

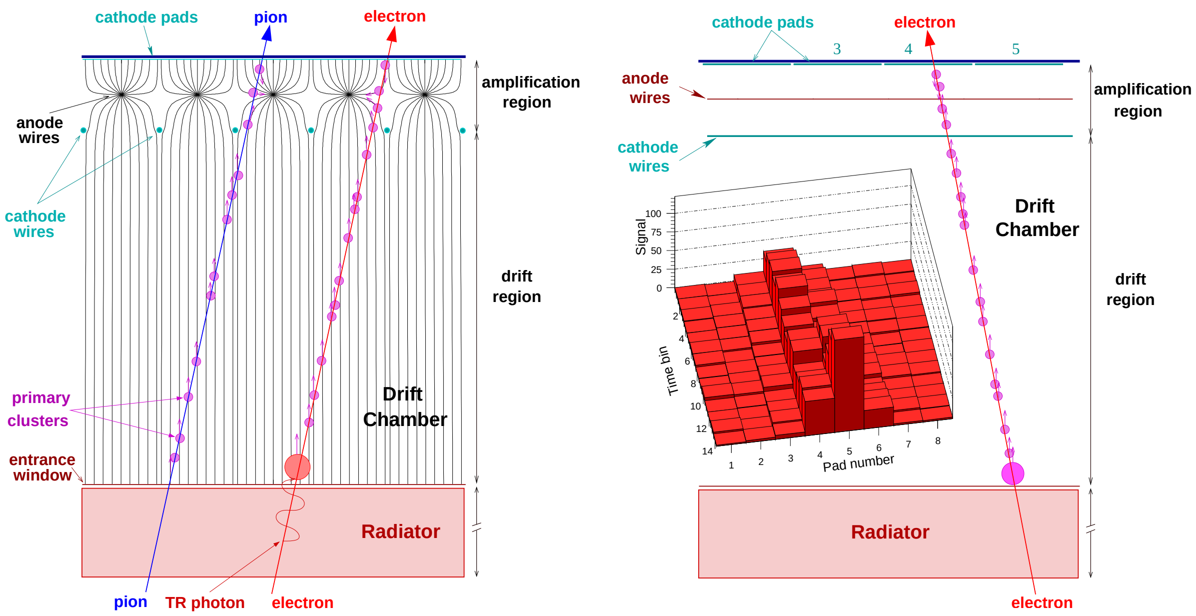

Figure 2.1: Left panel: geometry of a drift chamber module. An incident electron and a pion are compared. Right panel: principle of track reconstruction.

The image charge of the wire on the cathode pads is read out via charge sensitive preamplifiers/shapers (PASA) and Flash Analog to Digital Converters (FADC).

In the left panel of Fig. 2.1, we compare an incident electron to a pion. The electron, in contrast to the pion, creates a TR photon, which is emitted parallel to the track. In the chamber, this photon is rapidly absorbed; the gas mixture based on the high Z noble gas xenon was chosen to maximize the absorption cross section for photons at TR energies. To discriminate between electrons and pions, the increased charge deposit due to TR absorption can be used as an electron signature. Additional pion rejection is achieved exploiting the time dependence of the signal. The photon has a short absorption length in the chamber gas and is typically absorbed close to the entrance window. Since clusters produced farther from the amplification region travel a longer distance, TR is detected as a large peak at the end of the signal, as shown in the right panel of Fig. 2.1. Using the signal shape, pion suppression factors $\geq$100 have been measured for p=1 GeV/c at 90% electron efficiency: accepting 90% of all the electrons, less than 1% of the pions are misidentified as electrons.

In this diploma thesis, we investigate the position reconstruction performance of the TRD prototypes. The drift time of 2 μs (the time an electron from the entrance window needs to traverse the drift region) is sampled in several time bins. The present ALICE TRD design specifies 15 time bins of $\sim$135 ns width. The arrival time of the ionization corresponds to the track coordinate perpendicular to the pad plane. The resolution in this coordinate is determined by the time bin width. The charge sharing between the readout pads provides a second measure of the position of the ionization along the track. The pads are long and narrow rectangles with an average size of 7.25x87.5 mm^2. The anode wires are parallel to the smaller edge of the pads. They define the second coordinate. The charge induced on the cathode pad plane is shared by several pads, as can be seen in the right panel of Fig. 2.1. The fraction of the total charge induced on adjacent pads depends on the arrival position. We compare the charge deposit on neighbouring pads to determine the position of the ionization along the anode wire. In direction of the longer edge of the pad, the charge sharing is negligible, and along this coordinate no position reconstruction is performed.

During the development of the present design of the readout pads, an alternative pad shape has been considered and tested in beam experiments: chevron type pads. An appropriate choice of the chevron geometry allows to adjust the degree of charge sharing over a wide range of pad widths and anode-to-pad distances. On the other hand, chevrons require high precision during manufacturing of the pad plane and positioning of the anode wires. Any imprecision would lead to undesirable variations of pad response function and gain. Finally, the rectangular shape was adopted as a baseline for the TRD design, since the required charge sharing can also be achieved with this pad flavour. At present, a slight modification, consisting of a 2° tilt of the rectangle to a parallelogram, is discussed. That way, a measurement of the angle θ with better resolution than in the present design will be possible.

2.2 Prototype description

The dimensions of the prototype drift chambers are close to those anticipated for the final detector, except concerning the area, which is only 0.3$\times$0.2 m^2. We used 2 prototypes of different geometry and with different pad shapes: rectangular pads of 7.5 mm$\times$80 mm surface and 10 mm$\times$60 mm chevron type pads. A sketch of the different pad flavours is presented in Fig. 2.2.

For mechanical stability, the thickness of the pad planes is 3.5 mm. In both chambers, the cathode wires (Cu-Be, 75 μm diameter) have a distance ('wire pitch') of 2.5 mm. The anode wire (W-Au, 25 μm diameter) pitch is 5 mm. The wires are placed in a staggered geometry, as shown in Fig. 2.3. The anode-cathode gap (i.e. the distance from the anode wires to the cathode pads as well as to the cathode wires) is 3.5 mm in case of the chamber with rectangular pads and 2.5 mm in case of the chevrons pads. To have the same total depth for each chamber, the size difference of the amplification region is compensated by the length of the drift region, which is 28 mm for the rectanglar pads DC and 30 mm for the chevron pads DC. That way, both chambers have a depth of 35 mm. The dimensions have been adjusted to achieve a similar degree of charge sharing on the two pad types.

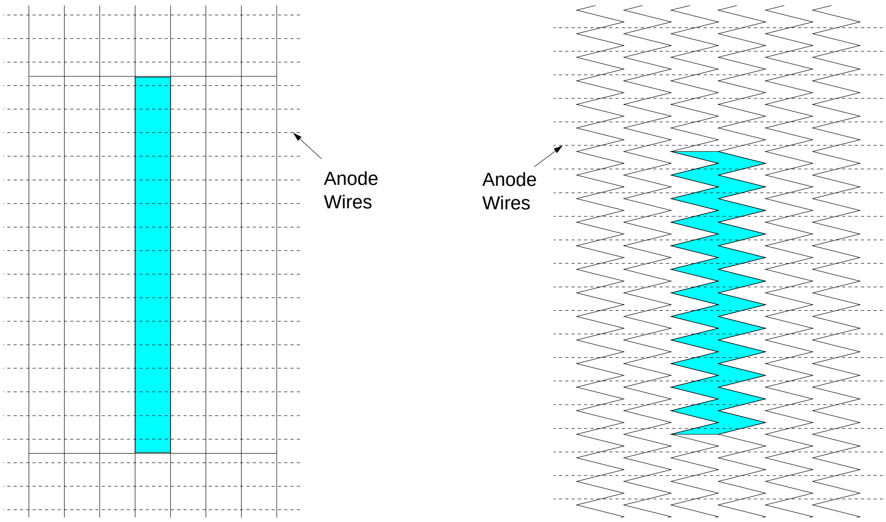

Figure 2.2: Different shapes of the readout pads: rectangular (left panel) and chevron type pads (right panel).

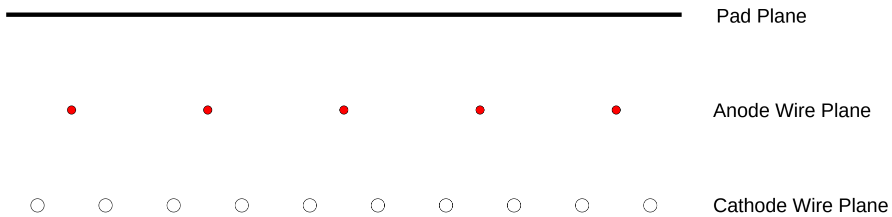

Figure 2.3: TRD readout chambers: wire geometry of the amplification region

2.3 Beam setup

In this work, we present results from test beam experiments performed in August and November 2001, at GSI and CERN. The measurements in August have been carried out at the 1 GeV/c secondary pion beam facility at GSI SIS. For this momentum, the natural electron contamination of the π^--beam (due to the conversion of photons from π decays in the production target) is of the order of 2-3% [10]. The setup for the beam test is sketched in Fig. 2.4. The following detectors were used:

- two drift chambers (DC) without radiator.
  DC1: rectangular pads, DC2: chevrons
- two scintillator counters (S1,S2)
- a gas-filled threshold Cherenkov detector (Ch), read out via a mirror by two photomultipliers, for electron identification

- a Pb-glass calorimeter (Lg), with dimensions 6x10 cm^2 and a depth of 25 cm for additional pion-electron discrimination
- two silicon microstrip detectors (SIM1, SIM2) with active area of 32x32 mm^2. Each has strips of 50 μm pitch in both horizontal and vertical direction, representing a total of 1280 channels per detector. They are used off-line as a position reference.

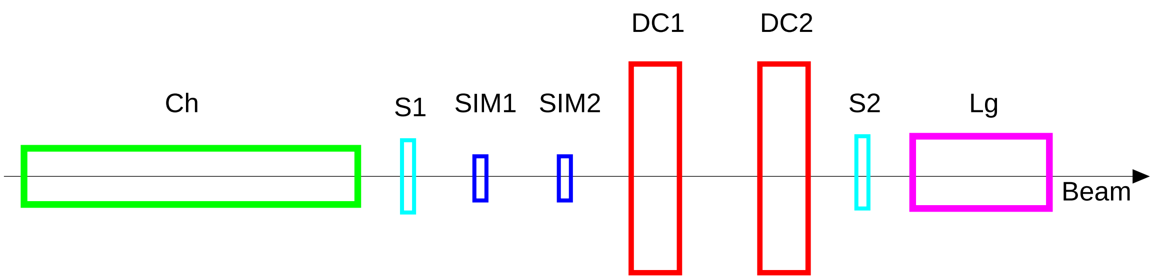

Figure 2.4: Sketch of the setup used for the beam tests (not to scale). The different components are explained in the text.

For the measurements of the TR performance of the prototypes, different radiators had been attached in front of the drift chamber. To study the position reconstruction capabilities of the detectors, it is sufficient to use pion tracks, and the runs dedicated to those studies were performed without radiators, minimizing the material in front of the chambers. Both detectors were operated with the ALICE TRD standard gas mixture of 85% Xe and 15% CO_2. The wires ran horizontally and the chambers were tilted along the wires to have a comparison of various angles of incidence. From each chamber, one horizontal row of 8 adjacent pads was read out using a discrete charge sensitive preamplifier/shaper (PASA) and a Flash Analog to Digital Converter (FADC) of 100 MHz sampling frequency, corresponding to a 10 ns time bin. To reduce the data flow, we recorded only 1 out of 2 or 3 (depending on the run) time bins, which increases the effective bin size to 20 or 30 ns. The data acquisition was the GSI standard, MBS [11], based on the VME event builder RIO2 [12]. The FADCs were connected to the event builder by a VSB bus.

The beam trigger was defined by the coincidence of the scintillator counters S1 and S2. In the off-line analysis, we use the information from the Cherenkov detector and the Pb-glass calorimeter to identify electrons in the sample.

Cherenkov light is produced by a charged particle, when its velocity $v = \beta c$ exceeds the velocity of light c/n of the traversed medium with refractive index n. All beam particles, pions and electrons, have equal momentum, p=1 GeV/c, which translates to different velocities $\beta = \sqrt{\frac{1}{1+\frac{(mc)^2}{p^2}}}$, due to the different masses of the two particle species (m_e=511 keV, $m_\pi \approx$140 MeV). Electrons, with β_e=0.99974, emit Cherenkov light, while the pions' velocity β_π=0.93659 is below the Cherenkov threshold (for a CO_2 filled detector) β_{thr}=0.99959 [5].

Electrons traversing the Pb-glass calorimeter produce cascades of photons and leptons, so called electromagnetic showers. In the high Z medium, they emit Bremsstrahlung photons with sufficient energy to create, in turn, electrons via pair production. The cascades develop through repeated interactions. When the average energy per secondary particle becomes low enough to stop further multiplication, the dominant energy loss processes are ionization for electrons and Compton scattering for photons [13]. Incident pions ionize the calorimeter medium. Their energy deposit is small compared to electrons, resulting in a lower signal. In Fig. 2.5, we present the correlation of the signal of of both detectors. Electrons and pions are well separated and a 2-dimensional cut, indicated by the lines, selects a clean sample of pions for further analysis. Due to the TR, the position resolution is slightly better for electrons than for pions. To present results independent of the pion-electron composition of the beam, in this work we use only pion data.

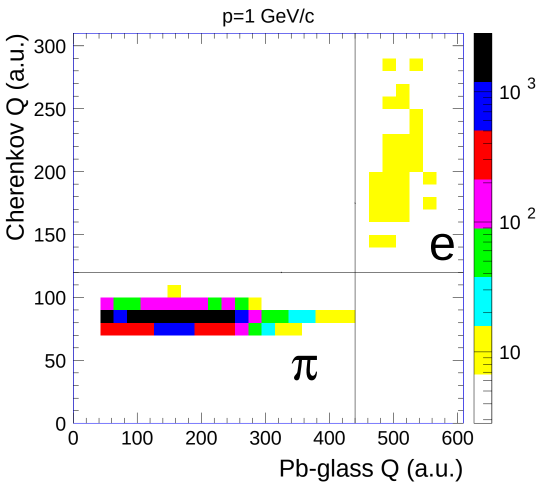

Figure 2.5: Correlation of the signals from the Cherenkov detector and the Pb-glass calorimeter. The thresholds used to separate negative pions and electrons are indicated.

The silicon microstrip detectors measure the position of the incident beam particles with high precision. Each of them consists of an n-type silicon crystal on which p-type strips with 50 μm readout pitch are mounted. An electric field is applied between the strips and the crystal. A particle traversing the depleted zone of the semiconductor deposits energy, exciting electrons into the conduction band. In the field, the electrons drift to the anode (the strip). The position of the strip with maximum charge measures the position of the hit. Evaluating the center of gravity of the charges deposited on adjacent strips, the position resolution of the SIMs was better than 100 μm [14]. Each detector has 2 crossed layers of strips, one on each side.

2.4 Average pulse height distributions

The shape of the signal, as sampled by the FADC, reflects the chamber geometry. Time distributions of the pulse height averaged over many events, $<$PH$>$, are shown in Fig. 2.6. The distributions in the left panel are measured for different values of the anode voltage U$_A$, which governs the gas gain. The time zero is arbitrarily shifted by about 0.3 μs to have a measure of the baseline. The peak at the beginning corresponds to the amplification region, where ionization from both sides of the anode wires contributes to the same time channel. The following plateau represents the drift region. In this zone of homogenous electric field, ionization electrons move towards the amplification region at constant drift velocity and arrive at constant rate. The tail at the end of the plateau results from build-up of detector currents from ion tails, convoluted with the finite PA response. The different heights of the distributions illustrate the increase of the gas gain with rising anode voltage.

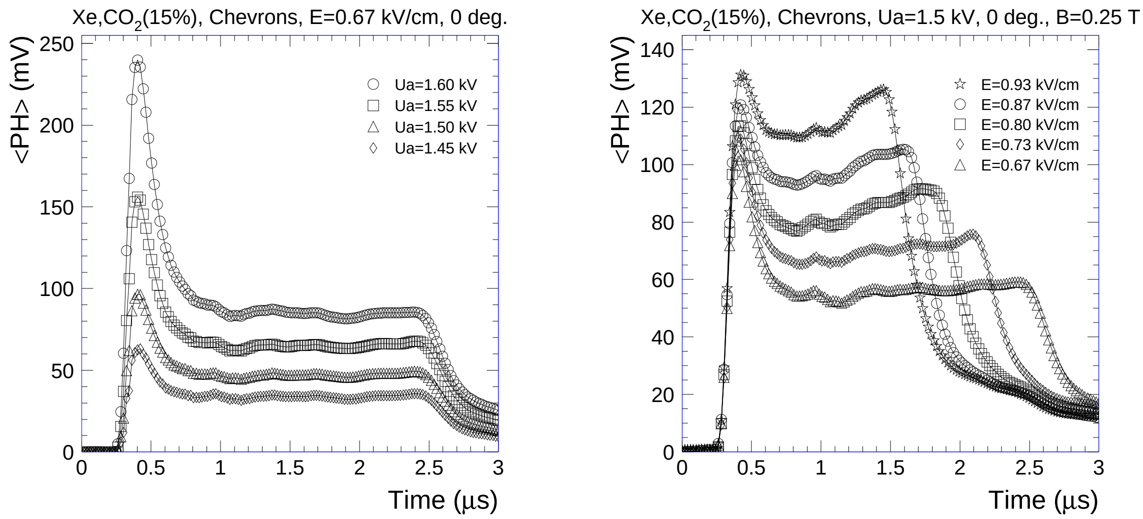

Figure 2.6: Average pulse height as function of drift time for different anode voltages (left panel) and different drift voltages (right panel).

In the right panel of Fig. 2.6 we present the average pulse height distributions for different values of the drift field. The field strength is varied via the drift voltage. A magnetic field of 0.25 T perpendicular to the electric field and to the beam incidence is applied. The fluctuations of the PH in the drift plateau are due to high noise in these runs. The height of the plateau strongly depends on the drift field: the drift velocity increases as function of the field, and the drift time, measured by the length of the plateau, decreases. Since the same amount of ionization is collected in a shorter time, the average PH has to be larger.

The applied drift voltage also affects the amplification peak: the peak becomes higher for increasing field. We interpret this behaviour as a consequence of the interplay of the electric fields in the passage from the drift to the amplification region. In the limit of zero cathode wire spacing, the amplification region would be perfectly isolated from the drift region, as is realized at the other side, where the pad plane serves as barrier. In an operating detector, drift and amplification region cannot be separated completely: the cathode pitch is of the same order of magnitude as the anode-cathode gap; the boundaries of the amplification region are far from symmetric. The ground level equipotential surface, which in the case of very close wires would exactly coincide with the cathode wire plane, is actually located in the drift region. A small part of the drift region, the size of which is determined by the applied drift voltage, contributes to the amplification peak, resulting in the observed variations of its height.

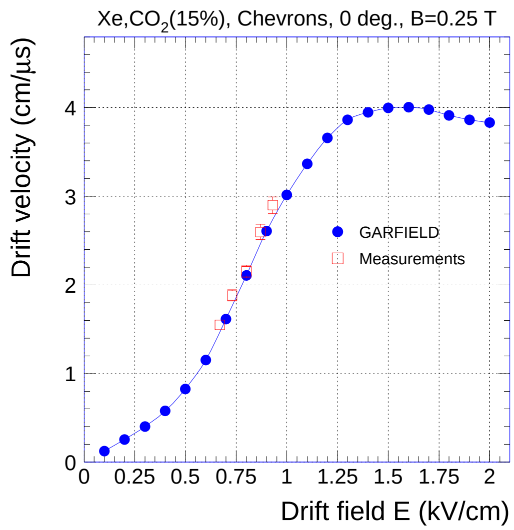

Figure 2.7: Drift velocity measured as function of the drift field for Xe,CO2(15%). The data are compared to GARFIELD/MAGBOLTZ [15, 16] calculations.

Analysis of the distributions presented in Fig. 2.6 allows a rough estimate of the drift velocities for different values of the drift electric field: we divide the geometrical drift length by the drift time, the length of the drift plateau in the $<$PH$>$ distribution. In the magnetic field, the drifting electrons move at an angle Ψ_L with respect to the electric field lines. This results in an increase of the distance travelled by the ionization electrons by a factor of $1/\cos\Psi_L$. We correct the drift velocities accordingly, using measurements of Ψ_L presented in chapter 4. For the small angles of about 5°, the correction is marginal. The results are presented in Fig. 2.7. The main limitation to the accuracy of the measurement arises from the imprecision in assigning the limits of the plateau, which we estimate to 0.1 μs. The results are in good agreement with GARFIELD/MAGBOLTZ [15, 16] calculations.

3 Position resolution: comparison of 2 drift chambers

In this chapter, we present results from beam tests of ALICE TRD prototype drift chambers, carried out at GSI SIS in August 2001.

In the development of the present TRD design, different readout pad shapes have been considered, chevron type and rectangular pads. We tested two prototypes, equipped with the different pad types. We compare the pad flavours in terms of point resolution and track reconstruction performance.

We investigate the impact of the FADC sampling frequency on the resolution, as well as the effect of the choice of the drift time interval for the angle fit. An important aspect of position measurements with a xenon operated drift chamber is the influence of the ion tail of the signal. We discuss the effect of an off-line tail cancellation on the position resolution of the chambers. Finally, a study of the resolution as a function of the angle of incidence of the primary particle is presented.

3.1 Position reconstruction

The distributions of average pulse height allow to determine the drift time interval, corresponding to the region of uniform motion of the ionization electrons. In this interval, we measure the position of the ionization along the track of the incident particle. The drift chambers provide two-dimensional point reconstruction within a horizontal plane: one coordinate, corresponding to the arrival time of the ionization, is perpendicular to the pad plane, the second coordinate is the displacement along the pad row, measured by the charge sharing between adjacent pads. The degree of charge sharing is measured by the pad response function (PRF), defined as the ratio of the charge deposited on the central pad to the total charge on all pads as function of the position of the hit relative to the pad center. To measure the PRF, we illuminate the chamber with a source of ^{55}Fe. This commonly used isotope emits mainly X-rays of 5.9 keV [5], an energy in the typical range of transition radiation. The photons are quickly absorbed by the detection gas. Each one creates a single ionization cluster close to the entrance

window, which travels along the field lines to the amplification region and arrives at a well defined point at the anode wire. The pulse heights on the pads are summed up over a time window of 1 μs to obtain a measure of the induced charge. The source is not collimated and the emitted photons cover a wide solid angle. For each event, the central pad is determined as the pad with the maximum charge. The position of the hit is reconstructed as follows:
we assume a Gaussian shape of the PRF, which can then be parametrised

$$\frac{Q_i}{Q_{i-1}+Q_i+Q_{i+1}} = Ae^{-\frac{x^2}{2\sigma^2}} = PRF(x)$$

where x denotes the distance of the hit from the center, and Q_i, Q_{i-1}, Q_{i+1} the charge on the center pad i and on the neighbouring pads on the left and on the right respectively (as a good approximation, we replace the total charge by the sum of 3 pads). For a hit at given x, the fraction of charge deposited on pad i-1, i and i+1 can be expressed in terms of the function values $PRF(x+W)$, $PRF(x)$ and $PRF(x-W)$, where W denotes the pad width [17]:

$$\begin{aligned}
\frac{Q_{i-1}}{Q_{i-1}+Q_i+Q_{i+1}} &= Ae^{-\frac{(x+W)^2}{2\sigma^2}} \\
\frac{Q_i}{Q_{i-1}+Q_i+Q_{i+1}} &= Ae^{-\frac{x^2}{2\sigma^2}} \\
\frac{Q_{i+1}}{Q_{i-1}+Q_i+Q_{i+1}} &= Ae^{-\frac{(x-W)^2}{2\sigma^2}}
\end{aligned}$$

We want to derive a measure of x independent of the a priori knowledge of the parameter σ. In a first step we write

$$\frac{Q_i}{Q_{i-1}} = e^{\frac{2xW+W^2}{2\sigma^2}} \tag{3.1}$$

$$\frac{Q_{i+1}}{Q_i} = e^{\frac{2xW-W^2}{2\sigma^2}} \tag{3.2}$$

Now we calculate the quantities

$$\frac{Q_{i+1}}{Q_{i-1}} = e^{\frac{2xW}{\sigma^2}} \tag{3.3}$$

$$\frac{Q_i^2}{Q_{i-1}Q_{i+1}} = e^{\frac{W^2}{\sigma^2}} \tag{3.4}$$

Solving Eq. 3.3 and Eq. 3.4 for x, we get

$$x \;=\; \frac{W}{2} \frac{ln\ (Q_{i+1}/Q_{i-1})}{ln\ (Q_i^2/Q_{i+1}Q_{i-1})}$$

The results are presented in Fig 3.1, for chevrons (left panel) and rectangles (right panel). We show the scatter plots along with a Gaussian fit to the mean of each channel in the interval [-1,1]. Both pad flavours exhibit very similar pad response functions. This had been the intention in the design of the chambers: for an equivalent PRF for rectangles and chevrons, the anode-cathode gap of the rectangular pads chamber had to be increased by 1 mm.

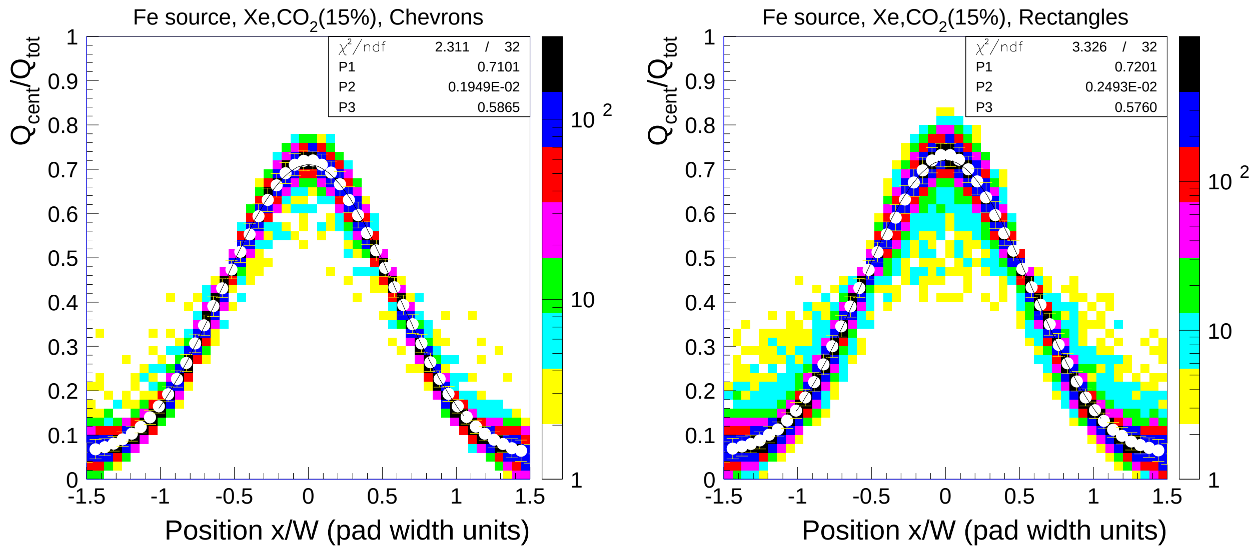

Figure 3.1: Measured pad response functions for chevrons (left panel) and rectangles (right panel). We show the scatter plots along with a Gaussian fit to the mean of each channel, plotted as dots, in the interval from -1 to 1.

Once the PRF is measured, one can determine the displacement x of the hit using pads $i{-}1$ and i (Eq. 3.1)

$$x \;=\; \frac{\sigma^2}{W}\, ln \frac{Q_i}{Q_{i-1}} - \frac{W}{2}$$

or, alternatively, pads i and i+1 (Eq. 3.2)

$$x \;=\; \frac{\sigma^2}{W}\, ln \frac{Q_{i+1}}{Q_i} + \frac{W}{2}$$

The best results are obtained by combinig these two measurements of x to a weighted average with weights w_1 and w_2 [17]:

$$x = \frac{1}{w_1 + w_2}\left[w_1\left(-\frac{W}{2} + \frac{\sigma^2}{W}\,ln\frac{Q_i}{Q_{i-1}}\right) + w_2\left(\frac{W}{2} + \frac{\sigma^2}{W}\,ln\frac{Q_{i+1}}{Q_i}\right)\right] \qquad (3.5)$$

Since the measurement error is roughly inversely proportional to the recorded pulses on the side pads, we choose $w_1 = Q_{i-1}^2$ and $w_2 = Q_{i+1}^2$.

For the study of the test beam data we use 65 time bins of 30 ns, if not mentioned otherwise. This interval spans the the full drift region of the DC. In Fig. 3.2 we present, for the downstream chamber (chevron pads), an example of the angle fit for one event. The pulse height distributions over 8 pads are shown in the left panel. The displacement relative to the center pad is calculated according to Eq. 3.5 for each time bin. Each bin corresponds to a slice in the drift region. Since the drift velocity in the drift region is constant, the displacement is ideally a linear function of time. The measured points, along with a linear fit, are shown in the right panel. The incident angle was 15° along the anode wires (across pads). It translates to an 8.0 mm deflection over the 30 mm drift length.

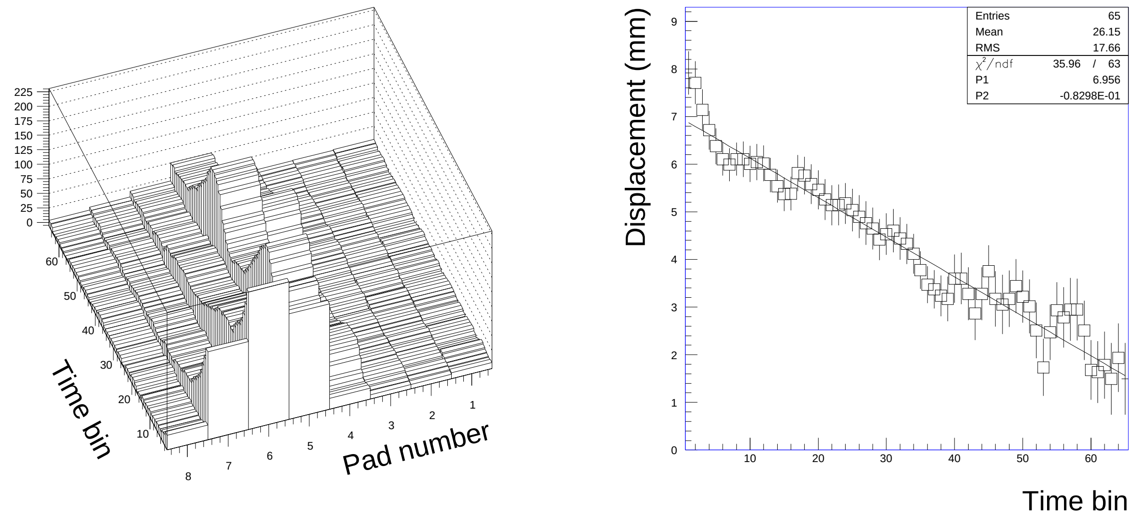

Figure 3.2: Left panel: the pulse height in the drift region versus time bin number on eight pads. Right panel: the displacement from the center pad as a function of time bin number.

The slope b of the fit ('$a + b \cdot t$') corresponds to the mean displacement along the pad coordinate per unit of time. It represents the incident angle of the primary particle: in case of zero degree incidence, when the beam axis is perpendicular to the pads, all ionization clusters from a track impinge at the same point of one pad. The displacement along the pad row is constant, the slope of the fit zero. At non zero angle of incidence, clusters from different parts of the track arrive at different displacement coordinates. We calculate the incident angle α according to

$$tan\,\alpha = \frac{b\,\cdot\,T}{D} \tag{3.6}$$

where D denotes the detector depth and T the drift time. The residuals of the fit, the difference between the reconstructed and the fitted value of the displacement at each time bin, contain information about the chamber resolution. We define the point resolution as the width a of a Gaussian fit to the distribution of residuals for all events. The angular resolution of the detector is defined by the width of a Gaussian fit to the distribution of reconstructed angles.

In Fig 3.3 we show a summary of the resolution as function of the signal-to-noise ratio, S/N. The signal is the average pulse height on the central pad per time bin in the drift time interval. It is equivalent to the mean pulse height of the drift plateau. We varied S/N via the anode voltage U_A. The drift voltage was kept constant, the drift times for both chambers (of different drift length) were adapted by tuning the drift velocities via the drift fields of E=0.71 kV/cm for the rectangles and E=0.76 kV/cm for the chevrons. The chamber tilt was 15°. At a similar noise level, the values of S/N reached by the chevron pads chamber are higher, due to its larger drift length.

The upper left panel of Fig. 3.3 shows, for both chambers, the average number of pads with a signal above threshold for each time bin, $\langle Npad\rangle$. The threshold is 2 times the noise value. $\langle Npad\rangle$ is in the order of 3 to 4 and increases with the signal-to-noise ratio. The high incident angle of 15° results in a large spread of the clusters over the pad row. The convolution of the charge distribution of the individual clusters with the spread of the arrival position of the clusters and the time response of pads and readout gives rise to the presented significant contribution of different pads (the charge from a single ionization, measured by the width of the PRF, is only spread over 2 to 3 pads). $\langle Npad\rangle$ is larger for the rectangles than for the chevrons. To understand the difference, we compare the pad flavours in terms of the the projection of a track onto the pad plane, normalized to the pad width, i.e. $\frac{D\cdot tan\,\alpha}{W}$. The ratio rectangles : chevrons amounts to 5 : 4, which explains the difference between the detectors. The observed evolution with S/N is a threshold behaviour. In the limit of very low S/N, the signal is dominated by statistical noise fluctuations, and the number of pads recording a 'signal' over threshold is independent of the pad characteristics. At higher S/N, the pad shape becomes more and more important.

In the upper right panel of Fig. 3.3, we present the average number of points used for the angle fit. The drift time corresponds to 65 time bins. For each bin, at least two pads are required to be above threshold. In case three pads are above threshold, a weighted mean of two measurements is used, as explained in the discussion of Eq. 3.5. Time bins which do not match these conditions are excluded from the fit, which leads

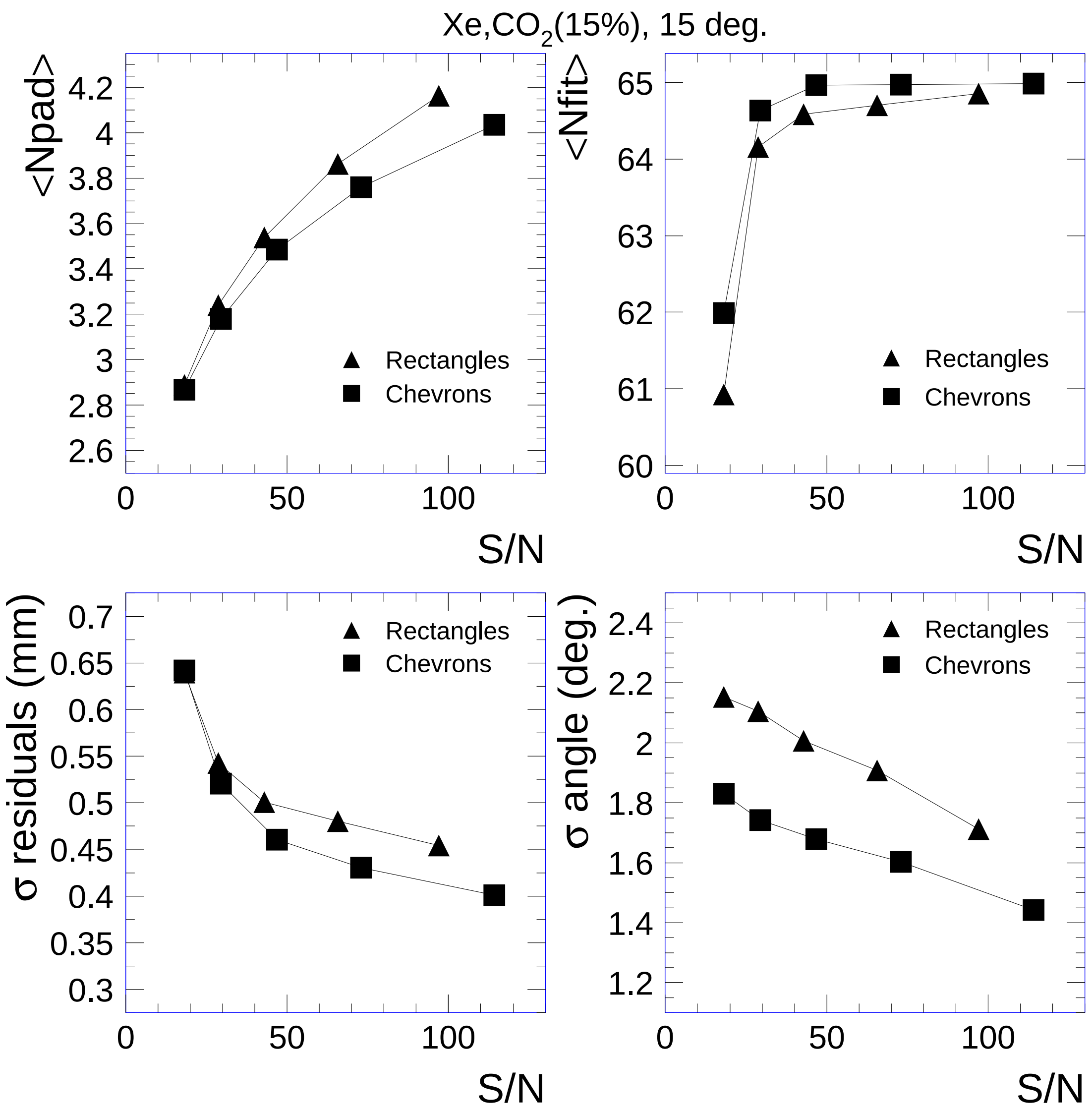

Figure 3.3: Position resolution as function of signal-to-noise ratio, S/N. Upper row: average number of pads with signal over threshold for each time bin, $\langle Npad \rangle$, average number of points used for the angle fit, $\langle Nfit \rangle$. Lower row: σ of Gaussian fit to the residuals and to the angle distribution.

to the increase of fit points with S/N. The difference between the two pad flavours is below 2%.

The lower row of Fig. 3.3 presents the position reconstruction performance. The point resolution, shown in the left panel, improves rapidly with increasing signal-to-noise for low S/N values and varies only slightly at very high values. In the limit of large S/N, the chevron pads, despite of their larger width, display a better point resolution (400 μm) than the rectangles (450 μm). We explain this as an effect of the ion tails. The most important contribution to the signal is produced by the movement of the ions. The massive ions move slowly, and the generated signal extends over a long time interval, inducing an important correlation among consecutive time bins. The corrupting effect of the tails on the position measurements is more important for the rectangular pads DC, which has a larger anode-cathode gap. The field in the proximity of the anode wire is very similar for both chambers, as the anode voltage was adjusted to equal gain. Increasing the gap from 2.5 mm (chevrons) to 3.5 mm (rectangles), one adds a considerable distance to be traversed by the ions, in the region of slowest drift, where the field falls off to zero.

We turn to the angular resolution, shown in the lower right panel of Fig. 3.3. Over the whole S/N range, the chamber with rectangular pads performs worse than the chamber equipped with chevrons. The reason is its smaller drift depth, which can be considered as a 'lever arm' for the angle fit. More quantitatively, we express the angle resolution σ_α as function of the point resolution σ_{point} and the number of (independent) fit points N_{fit} [17]:

$$\sigma_\alpha \simeq \sqrt{\frac{12}{N_{fit}}} \cdot \frac{\sigma_{point}}{D} \tag{3.7}$$

Smaller detector depth D leads to worse angular resolution. The qualitative agreement of the results with Eq. 3.7 can not be corroborated quantitatively: the difference of typically 0.25°, an effect in the order of 15%, exceeds the 7% difference in D (D=28 mm for the rectangles, 30 mm for the chevrons). Furthermore, with regard to Eq. 3.7, one expects a similar dependence of angular and position resolution on the S/N ratio. But the curves display a very different shape. These discrepancies are due to the effect of the ion tails on the angle resolution, as will be demonstrated in section 3.3.

Relating the measured angular and point resolution for a given S/N, Eq. 3.7 provides an estimate of the number of independent fit points. We obtain values of the order of N_{fit} = 3.3 to 5.4 points, decreasing for higher values of S/N. This is in marked contrast to the number of $\sim$65 points actually used for the fit. The drastical difference indicates the high degree of correlation between subsequent position measurements. We investigate the effect of the reduction of the number of fit points on the position resolution: out of the original 65 samples only 32, 21, . . . , down to 13 samples are used, skipping samples and consequently increasing the width of one time bin from 30 to 150 ns. The results are shown in Fig. 3.4 for the rectangular pads chamber. Although in the rebinning procedure information is lost, in most of the cases we find a small ($\sim$5%) improvement of angular and position resolution by the reduction of fit points. Clearly, the position reconstruction performance profits from the decoupling of the fit points by the rebinning process. At low S/N, the reduction of the number

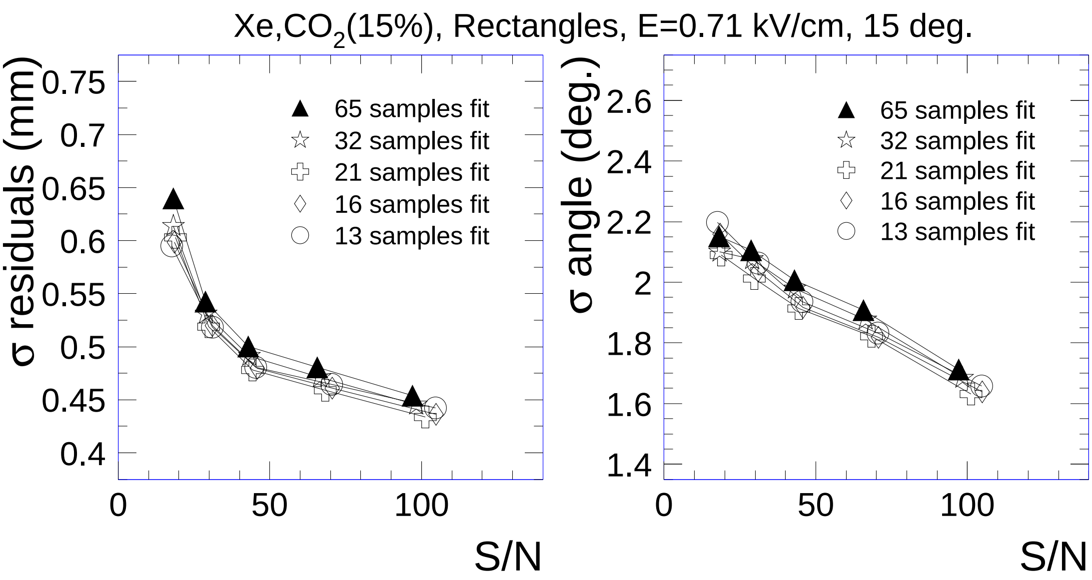

Figure 3.4: Influence of the binning on the position resolution.

of samples makes the angle fit very sensible to noise fluctuations, leading to strong relative variations of the number of points used for the angle fit. This results in the observed degradation of the angular resolution, according to Eq. 3.7. Since the fitting algorithm optimizes the residuals, the position resolution profits from this reduction (in the - hypothetical - limit of two fit points, the residuals are zero, but the angle is completely subject to the PH fluctuations).

Reducing the number of samples, the corresponding curves are shifted towards higher S/N. With larger time bin width, the first bin of the drift plateau, centered at $\sim$0.68 μs, extends slightly into the amplification peak, and the mean pulse height increases. In the following section 3.2, we show that angular and point resolution suffer from an extension of the drift time interval into the amplification peak. This may explain, why at high S/N the resolution is optimal for the 21 samples fit and becomes somewhat worse for higher binning. We also note that wider samples reduce the time interval used for the fit, since the centers of the first and last time bin used for the fit are shifted to later and earlier times, respectively. This translates into a smaller lever arm for the angle fit, which is unfavourable for the angle resolution.

The most important effect of the variation of the number of samples we observe is the improvement of the resolution with coarser sampling, as a result of the reduced correlation between the wider time bins. Clearly, we need to cope with the influence of the ion tails. With respect to properties of the numerical deconvolution procedure to be presented below, for further studies we use the minimum time bin width.

3.2 Influence of the choice of the fit range

The angle fitting procedure requires the assignment of the limits of the drift time interval, based on the time distribution of average pulse height. The choice of these limits is not unambiguous, and for this reason we investigate the effect of variations of the drift interval on the position resolution. In Fig. 3.5, we present the average pulse height distribution. The drift time interval of 1.93 μs used so far is indicated as 'original choice'. Several steps of shrinking and expanding the interval are performed, at the beginning (amplification peak) as well as at the end of the plateau. The maximal deviation from the original choice is 8%. The variations at the end of the plateau are labelled in terms of positive fractions of the original drift length, variations at the beginning are given as negative ratios.

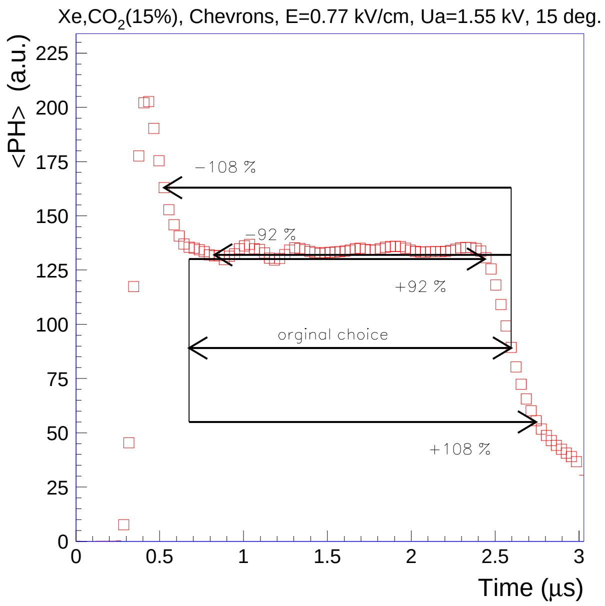

Figure 3.5: Shrinking and Expanding the drift region: different intervals of time bins to contribute to the angle fit. For given start of the plateau at 0.67 μs the end (originally chosen at 2.6 μs) is varied and vice versa. The resulting length of the plateau is given as a ratio of the original choice. We use positive numbers for the variation of the end of the plateau and negative numbers for variation at the amplification peak.

In Fig. 3.6, the effect on the reconstructed angle (upper row), on point (central row) and on angular resolution (lower row) are shown. First we discuss the right hand panels, corresponding to variations at the end of the plateau, which is dominated by tails of the signal. Since the fit points are weighted with their pulse height, points from this region have only weak impact on the slope of the fit. Given a constant slope, the reconstructed angle increases linearly with the length of the drift time interval, following Eq. 3.6 (D is not rescaled). This behaviour is seen in the upper right panel: an extension of 8% results in an 8% increase of the angle. The variation of the residuals with the choice of the end of the drift is only marginal, less than 20 μm. The angular resolution improves with longer drift, possibly as an effect of the increasing number of fit points. The effect is less than 0.1°.

The situation is different at the amplification peak (left column of Fig. 3.6), where the signal is typically higher than the average, and the contribution to the fit is more important. The beginning of the drift plateau corresponds to the passage between drift and amplification region with its very particular field configuration. The variation of the reconstructed angle is smaller than the drift length variations. This points to a reduced drift velocity. As expected, the effect on the point as well as angular resolution is more pronounced for the extension of the drift than for truncation. The influence of the variations at the beginning of the plateau is stronger than for variations at the end of the drift. The change of point resolution is less than 50 μm, the variation in angular resolution is 0.1°.

Drastic variations of the adopted limits of the drift time interval lead only to small variations of the position resolution. The situation is different for the value of the reconstructed angle, which depends explicitly on the drift time.

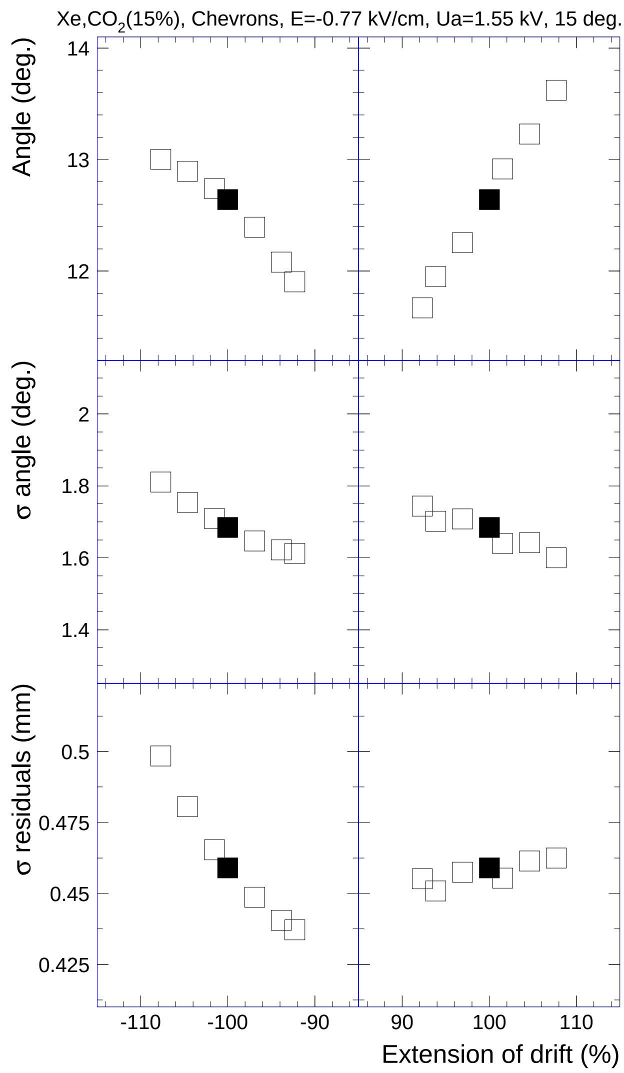

Figure 3.6: Influence of the choice of the limits of the drift region on the angle reconstruction and position resolution. The time interval used for the angle fit is varied at the beginning (left panels) and the end (right panels) of the plateau. The extension of the plateau is given in terms of the originally adopted choice, the numbers on the abscissa refer to Fig. 3.5. Results are presesented for the reconstructed angle (upper row), angular (central row) and point resolution (lower row).

3.3 Influence of the ion tails

In the amplification process, ions are created in the avalanche around the anode wire. Their mobility is typically by a factor 1000 smaller than the mobility of electrons. During their slow drift to the cathode pad plane, they induce a slowly rising signal on the anode, recorded by the pads, which translates into a tail after the amplifying/shaping by the PASA. The tails lead to a strong correlation among subsequent time bins, making the position resolution performance very sensitive to Landau fluctuations of the charge deposit. Since the drift velocities of xenon ions are particularly small compared to more commonly used gas compositions, we face a drastical influence of ion tails, convoluted with the finite PASA response. In Fig. 3.7 we give an example of the correlation of the reconstructed angle with the shape of the individual signal. The left panel shows two (extreme) cases, in which the signal is predominantly at the beginning or at the end of the drift time (expressed as time bin number). The arrows mark the drift time position of the center of gravity of the signal, $t_{\langle Q \rangle}$, for each case. The right panel shows, for both cases, the displacement distributions, along with the fits. In case of larger clusters at the beginning of the drift (squares), the reconstructed angle is much smaller compared to the case with large clusters later in time (dots). In the first case, an important fraction of the time bins used for the fit is contaminated by the tails of preceding clusters.

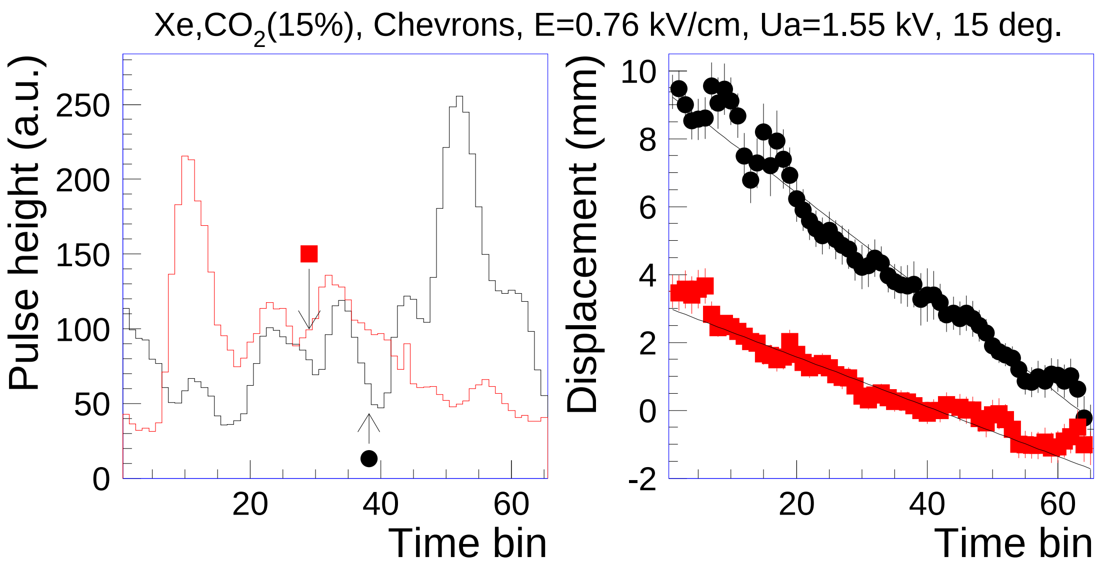

Figure 3.7: Left panel: two examples of the pulse height in the drift region summed up over all pads. The mean of each distribution is marked. Right panel: the displacement from the center pad as a function of time bin number and the result of the fit for the two events of the left panel.

The effect on the angle reconstruction is shown in Fig 3.8, in the upper left panel. We correlate the reconstructed angle to the center of gravity of the signal, $t_{\langle Q \rangle}$. The average values of the angle for each slice in $t_{\langle Q \rangle}$ are overlayed as dots. The beam incidence was 15° with respect to the normal to the pads; the studies are performed for a moderate value of S/N$\simeq$40. The reconstructed angle is systematically smaller in case of events with large clusters at early time. At high $t_{\langle Q \rangle}$, the values saturate.

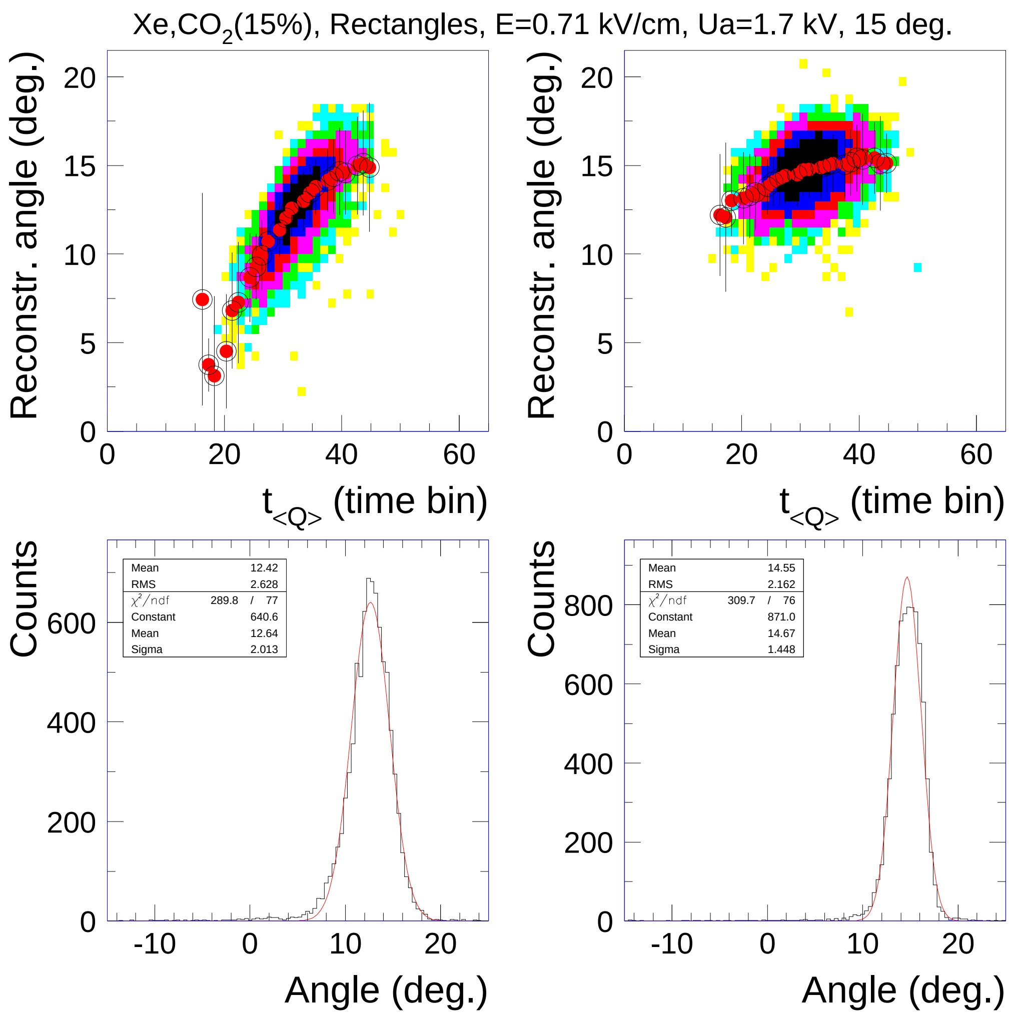

Figure 3.8: Angle reconstruction before (left panels) and after (right panels) deconvolution. In the upper row we show the distributions of reconstructed angle vs. position of the mean charge deposit in the drift time, $t_{\langle Q \rangle}$. The average values are averlayed as dots. In the lower row we compare the angle reconstruction performance. The incident angle is 15°.

To cope with the effects of the detector response on the position reconstruction, we apply a so-called 'tail cancellation', namely substracting the known signal tail as a function of time. Originally, this cancellation was proposed at the level of the analog electronics (PASA) [18]. As demonstrated in appendix A, the operation is equivalent to de-convoluting the Laplace transformed signal with the following transfer function [18]:

$$f(s) \;=\; \frac{s+1/\tau}{s+k/\tau} \tag{3.8}$$

We applied such a deconvolution (under the form of a numerical approximation, presented in appendix A) in the off-line analysis. The constants k and τ are k=1.54 and τ=1.2 μs. In Fig. 3.8, we plot in the upper right panel the reconstructed angle, obtained after tail cancellation, as function of $t_{\langle Q \rangle}$. The correlation is drastically reduced (although not completely removed). The events with small $t_{\langle Q \rangle}$ values, which suffer most from ion tails, are considerably affected by the deconvolution: the reconstructed angles are larger than without the tail cancellation. In the lower row of Fig. 3.8, we compare the angle distributions without (left panel) and with (right panel) deconvolution. The angular resolution, measured by the σ of the Gaussian fit, is clearly improved. Note, that also the mean value of the reconstructed angle is shifted. The measured value 14.7° is in good agreement with the nominal incidence of 15±0.5° (the errors reflect the limits of accuracy of placing the chamber at a given angle).

From the correlation plot in the upper right panel also the limitations of the method become clear. Even after the deconvolution, a remnant evolution of the average values for the different slices as function of $t_{\langle Q \rangle}$ is visible. The correlation between subsequent time bins can not be completely removed. This demonstrates the imperfection of our procedure of tail cancellation and more fundamental restrictions to the time response

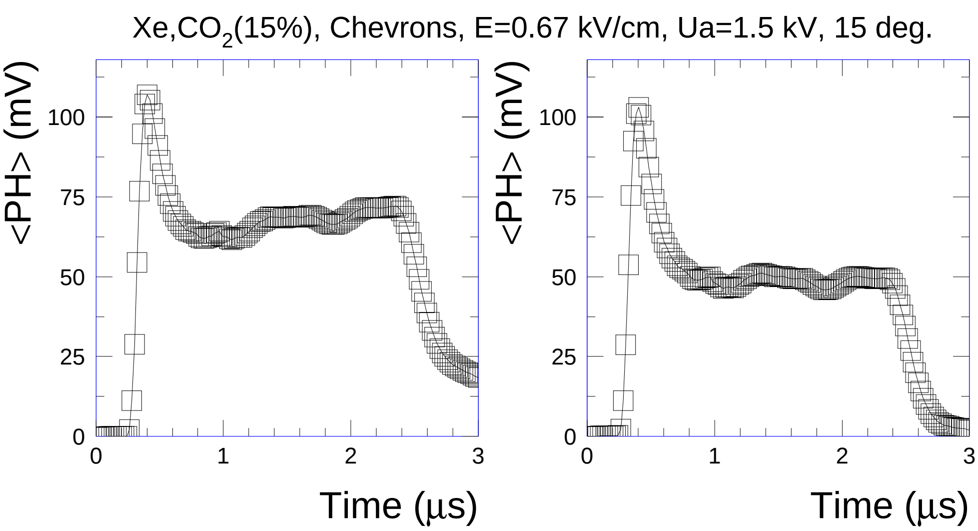

Figure 3.9: Average pulse height as function of drift time before (left panel) and after (right panel) deconvolution.

of the detector and readout. In the fully developed ALICE readout chain a more sophisticated deconvolution in several steps will be performed by a digital filter.

In Fig. 3.9, we present an example of the average pulse height as function of the drift time before (left panel) and after (right panel) the tail cancellation. Two effects of the cancellation are seen: i) the originally slightly rising plateau is made perfectly flat; ii) the average signal in the drift region is reduced by about 30%.

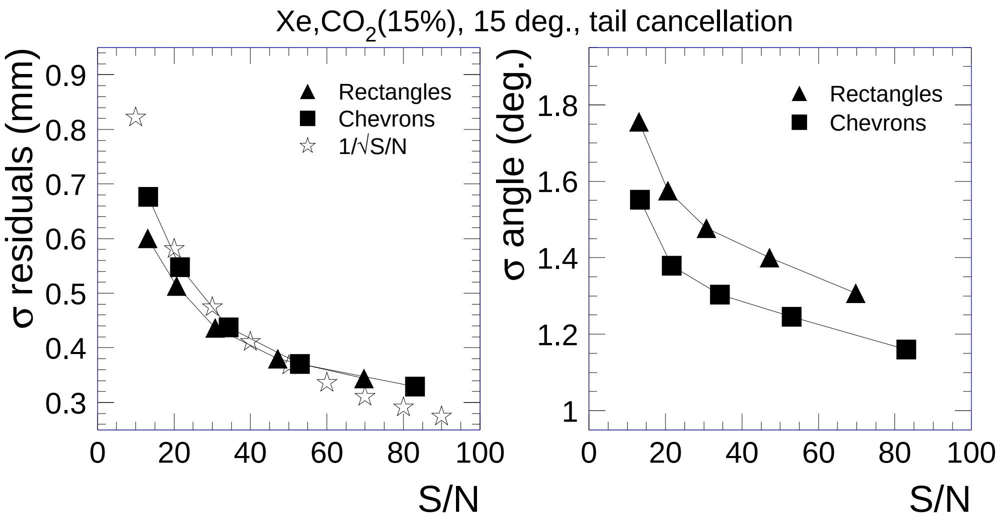

Figure 3.10: Position resolution of the drift chambers after deconvolution. Left panel: point resolution. Right panel: angular resolution.

Once again, we turn to the position reconstruction performance of the two chambers as function of the signal-to-noise ratio. We apply tail cancellation. In the left panel of Fig. 3.10 we show the point resolution of the drift chambers, along with an 1/$\sqrt{(S/N)}$ function, arbitrarily normalized. The shift of the height of the drift plateau reduces the average signal, leading to lower values of S/N compared to Fig. 3.3. We observe an improvement of the point resolution, values down to 330 μm are reached. The deconvolution removes the differences in the performance of both chambers. The rectangular pads chamber, suffering stronger from the ion tails, exhibits now even a slightly better resolution (as one expects from the smaller width of the rectangular pads).

The shape of the curve of the angle resolution as function of S/N, in the right panel of Fig. 3.10, is drastically modified by the deconvolution. The resemblance to the residuals curve is now obvious. In the limit of high S/N, angular resolutions of about 1.3° and 1.15° are achieved for rectangles and chevrons respectively. The difference of $\sim$10% in the angle reconstruction performance can be explained as an effect of the 7% drift length difference.

In Fig. 3.11, we compare the influence of the time bin width on the position reconstruction, applying tail cancellation. The point resolution (left panel) displays very small overall variations. At very low S/N, it benefits from the reduction of the number of fit points, whereas the angular resolution (right panel) becomes worse. We observed a similar effect in the case without tail cancellation (compare Fig. 3.4). With increasing S/N, the curves for diffent number of samples approach each other, the evolution of the point and angular resolution is governed by the S/N ratio.

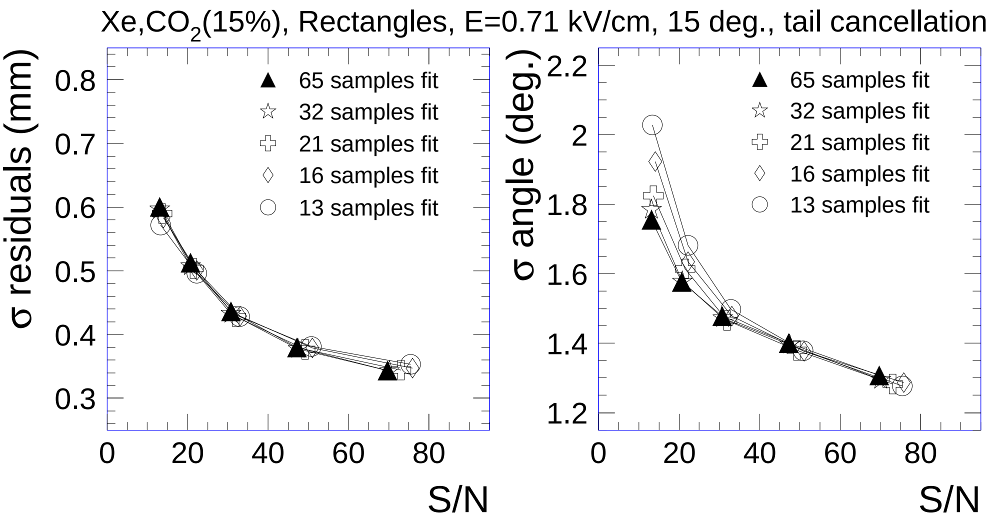

Figure 3.11: Influence of the binning on the position resolution. Deconvolution of the signal is applied.

So far, all studies of the influence of the signal-to-noise ratio have been performed at a given value of the drift field for each chamber. S/N was varied by changing the anode voltage U_A at fixed drift voltage. We turn now to the influence of the drift field, considering variations of S/N by the compression of the signal with higher drift voltage U_D. In Fig. 3.12, we plot the position resolution as function of S/N variations at constant gain (constant anode voltage), along with the previously discussed results for S/N variations at constant drift voltage. The results are obtained with tail cancellation. The point resolution, presented in the left panel, exhibits no dependence on the way the S/N variations are achieved. The points for different U_D are well on top of the curve for the U_A variations. The angular resolution, in the right plot, behaves different: compression of the drift plateau, although increasing the S/N ratio, leads to a degradation of the resolution. It suffers from the reduction of the number of fit points in the shorter drift time interval and the increasing influence of the ion tails, as those are compressed along with the drift plateau.

From the results presented above, the position resolution is expected to exhibit a strong dependence on the angle of incidence. In Fig. 3.13 in the upper left panel, we

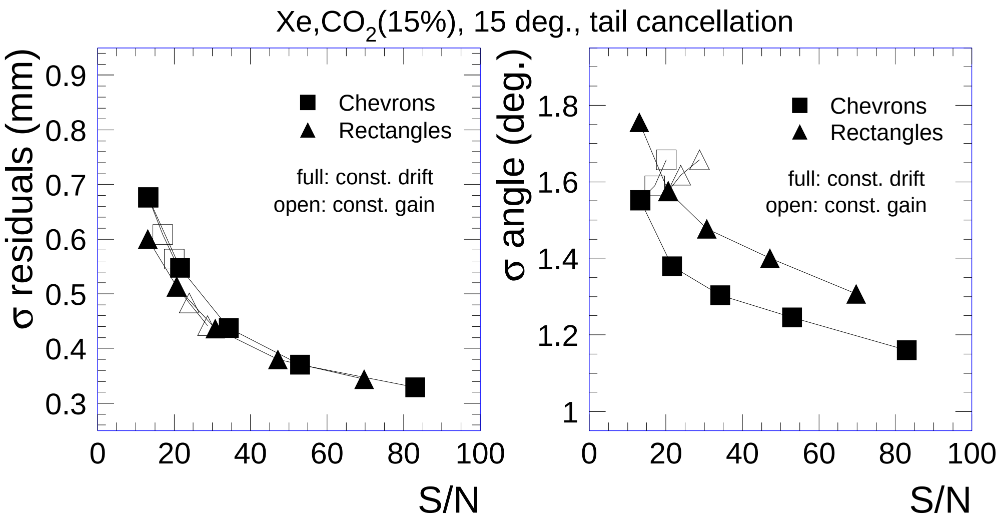

Figure 3.12: Position resolution of both chambers. We increase the signal-to-noise ratio by increasing U_A at constant drift field (full symbols) or by compressing the signal via increase of the drift field at constant gain (open symbols).

present the angular resolution as function of the measured incident angle. For these studies a smaller time bin of 20 ns has been used, providing 97 position measurements for the angle fit. Without correction (open symbols), we observe a significant evolution of the angle resolution, from $\sigma\approx 0.7^\circ$ at an incident angle of 0° to $\sigma\approx 2^\circ$ at 15° incidence. The effect is reduced by tail cancellation (full symbols): at high angle of incidence, the angular resolution benefits from the tail cancellation, at low incidence, the resolution suffers from the S/N reduction. The measurements have been carried out at a S/N ratio of about 20 (uncorrected points). At such low S/N, the angle of intersection between the curves of the corrected and uncorrected points is relatively high. In the upper right panel of Fig. 3.13 we illustrate the situation at higher S/N (S/N$\approx$40 for the uncorrected points): the resolution improves, both curves are shifted down and intersect at a smaller angle. These measurements have been performed with a prototype DC with identical geometry, equipped with chevron pads of equal width (but smaller height, resulting in a reduced total surface of (4.5 cm^2), see [2], Chapter 14).

In the lower row of Fig. 3.13, we show the point resolution as function of the angle of incidence. In the case of low S/N (left panel) and for the uncorrected data, there is no such drastic evolution as in case of the angle resolution. From the lowest incidence to an angle of 4° there is even a slight improvement, which can be explained by the increase of the signal-to-noise with higher chamber tilt, as the segment of the primary particle track within the chamber volume is longer at higher beam incident angle. At low overall S/N, small variations are of large impact on the position resolution. For the corrected data, these variations result in an improved resolution at high incidence compared to low incident angle. The angle of intersection between the curves of corrected and uncorrected points is higher than in the analog plot of the angle resolution. This can also be observed for higher S/N, where the intersection angle of both curves is 11° for the position resolution (lower right panel) and 4.5° for the angular resolution (upper right panel). At high S/N, the point resolution is more similar to the curve of the angle resolution: at small angle of incidence, the point resolution suffers from the S/N losses by the tail cancellation, whereas at high incident angle it is improved by the correction.

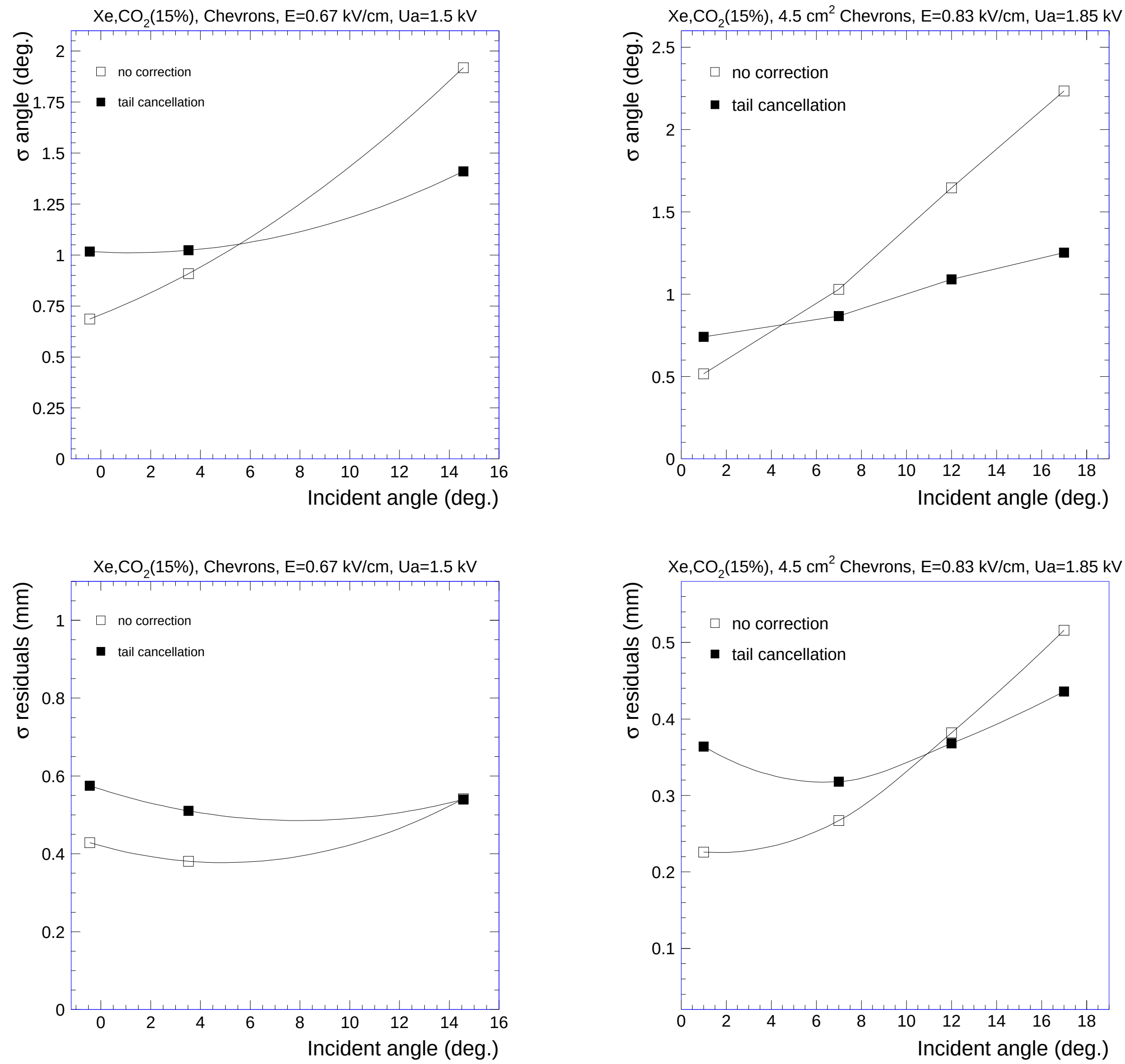

Figure 3.13: Upper row: angle resolution as function of the angle of incidence with and without tail cancellation. Lower row: point resolution. We compare results for the 6 cm^2 chevrons (left column) to results at higher S/N for chevron pads of 4.5 cm^2 surface (right column).

4 Position resolution: measurements in a magnetic field

In the beam time in August 2001, we operated one drift chamber in a magnetic field. These runs represented the detector's working conditions: ALICE TRD will operate in the field of the L3 magnet. The field at GSI, created by coils in a Helmholtz geometry, was highly nonuniform, and we present finite element calculations to analyse its configuration. In our measurements, we deal with various aspects of the influence of a magnetic field on moving charged particles. The most obvious effect is the distortion of the beam trajectory. The drifting ionization electrons are influenced too. They move at an angle with respect to the electric field lines, called Lorentz angle. Since the drift chamber superimposes this angle on the incidence, its knowledge is important for the TRD data analysis, particularly at the trigger level. The Lorentz angle depends on operation parameters of the drift chamber and on the gas composition. Our measurements allowed to determine this quantity for Xe,CO_2(15%) for the first time experimentally.

In the process of ionization of the detector gas by the incident particle, a small fraction of highly energetic electrons is produced. These δ-electrons distort the position resolution. In a magnetic field, they curl up around the B-field lines, and the resolution is expected to improve. We present the effects of the magnetic field on the resolution of the drift chamber under various operating conditions.

4.1 Configuration of the magnetic field

To produce a magnetic field at GSI, two Helmholtz coils with an inner radius of 13.5 cm, an outer radius of 32.1 cm and a thickness of 4.4 cm were installed. The centers of each coil were aligned to a common vertical symmetry axis, separated by 32.9 cm. The beam axis crossed this symmetry axis midway between the coils. The current through the 72 windings of each coil had values of $\pm$500 A, $\pm$1000 A, $\pm$1250 A and $\pm$1400 A. Given the limited space between the coils, we could not operate both chambers in the field simultaneously and restricted our measurements to the chevron pads DC. A sketch of the setup is shown in Fig. 4.1. The silicon microstrip detectors were placed

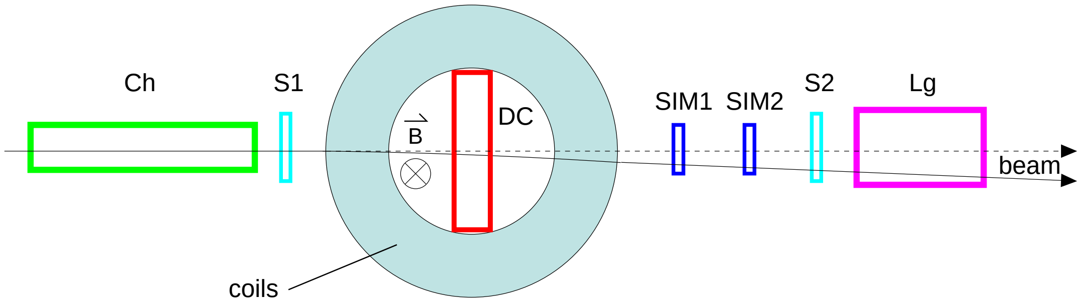

Figure 4.1: Setup of the magnetic field measurements (top view). One drift chamber is placed between coils. The deflection of the negative pion beam in the magnetic field is sketched.

downstream the coils, at a distance of 38.1 cm to the chamber and 25.0 cm between each other. The π^- beam is deflected by the field, as schematically indicated.

To determine the values of the magnetic field for the different currents, we used OPERA, a tool to analyse electro- and magnetostatic problems using finite element calculations. The implementation of the setup in the program, along with contour lines of the field for a current of 1250 A, is shown in Fig. 4.2. The symmetry of the setup allows to reduce the configuration to two dimensions and implies the use of cylindrical coordinates. The labelling of axes in OPERA differs from the physics standard notation. 'R' denotes the radial axis. It is the direction of beam incidence, and the chamber depth is measured along this coordinate. From the symmetry it is clear, that the magnetic field lines are vertical, in direction of the height Z. The plot shows a cross section of the two coils and lines of constant B_Z in the interval 0.19 T$\leq B_Z \leq$0.3 T. The pad row in the center between the coils, at R=0 and Z=0, was read out. At this point, currents of 500 A, 1000 A, 1250 A and 1400 A produce fields of B_Z=0.1 T, 0.2 T, 0.25 T and 0.3 T respectively. The OPERA calculations of the field were checked by measurements.

Fig. 4.3 shows the variations of the magnetic field in more detail. In the upper panel, we plot the B_Z component for points on the beam axis. In the interval from 0 to $\sim$2 cm, corresponding to half the depth of the chamber, the field is practically constant. For Z$\geq$10 cm, the field strength quickly ceases and takes a negative value for Z$\geq$36 cm. For higher Z, the long range field approaches zero asymptotically.

In the lower panel, we plot B_Z along the vertical Z-axis. The field grows with increasing Z, approaching the coils. We estimate the error on the nominal value of the magnetic field, at R=0, Z=0, for incident beam particles. This error arises from the angular spread of the beam and the imprecision of the exact position of the beam spot. We consider variations of the field strength at the surface of the center pad: these are stronger along Z than along R. In addition, the uncertainity about the vertical position of the beam spot, corresponding (in the most pessimistic estimate) to the height of one reaout pad of 6 cm, is large. In the interval -0.06$\leq$Z$\leq$0.06 the field strength variation is 7% of the nominal value at Z=0, a tolerable deviation.

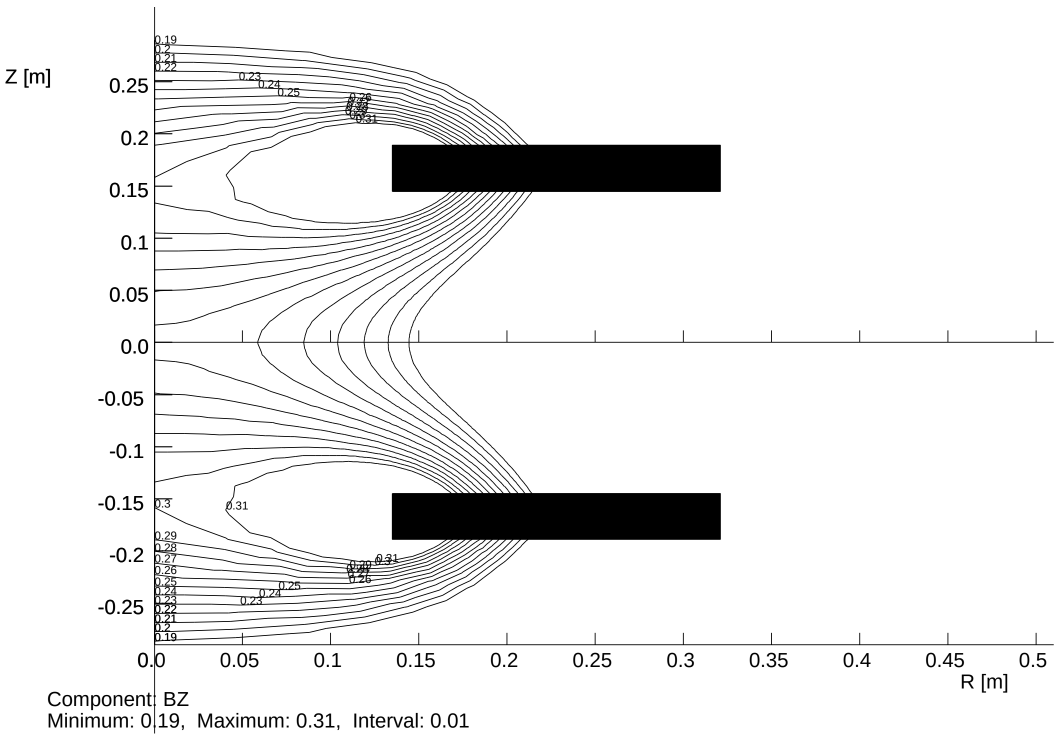

Figure 4.2: Contour lines of constant B_z.

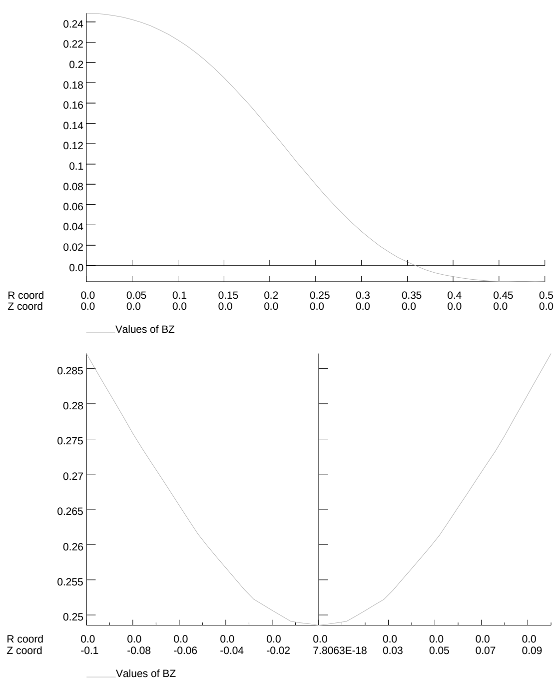

Figure 4.3: Values for B_Z along the particle incidence (upper panel) and along the vertical symmetry axis z (lower panel). Abscissa values are in meters.

4.2 Deflection of the beam trajectory

The charged beam particles moving in the magnetic field feel the Lorentz force. In Fig. 4.4, in the left panel, we present the trajectory calculated by OPERA for 0.25 T. We show the projection of the trajectory on the horizontal plane Z=0; the vertical deflection, out of this plane, is negligible. The units are in meters. The beam axis is parallel to the abscissa, and we plot 6 incident particles with an energy of 1 GeV arriving from the right. They move on practically straight trajectories until they approach the center. The most significant deflection takes place in a zone of about ΔR=15 cm around the symmetry axis, defined by the inner radius of the coils. The total deflection, the angle of the trajectory with respect to the incidence in field-free space, is 1.37° according to OPERA.

This beam deflection is measured by the silicon microstrip detectors (SIM). We evaluate for each event the difference Δx between the horizontal coordinates x_1,x_2 measured in both SIMs: Δx = x_2-x_1-Δx_0. The offset Δx_0 is due to the unavoidable misalignment of the two detectors. It is determined in the B=0 runs, with 0 beam deflection. For each event, we calculate the incident angle α, dividing Δx by the distance d between the SIMs: tan α = $\frac{\Delta x}{d}$. The angle distributions for B=0 and B=$\pm$0.25 T are presented in the right panel of Fig. 4.4. The B=0 case defines the calibration, so the mean angle is exactly 0° in this case. For B=$\pm$0.25 T, we measure a beam deflection of +1.672° and -1.688 $^\circ$ (mean of the distribution). The RMS of the measured angle distribution of $\sim$0.4° reflects the spread of the beam.

The measured values of the deflection angle are higher than the angle of 1.37° calculated by OPERA for a particle in the field free region. In fact, the program predicts a field of long range, which is small but not zero at the silicon detectors (which are at a considerable distance of circa 0.5 m from the coils). A more precise calculation of the beam deflection between the silicons, taking the curved shape of the trajectory between the silicon detectors into account, results only in a slightly modified prediction of 1.44° for the angle between the silicons, a correction of 5%: the curvature of the trajectory is very small, and it is justified to regard the silicon measurements as values of the beam deflection in field-free space, despite of the discrepancy between measured and predicted value. This discrepancy is possibly due to the increase of B$_Z$ in horizontal direction towards the coils, leading to a larger deflection for particles which do not exactly pass through the center.

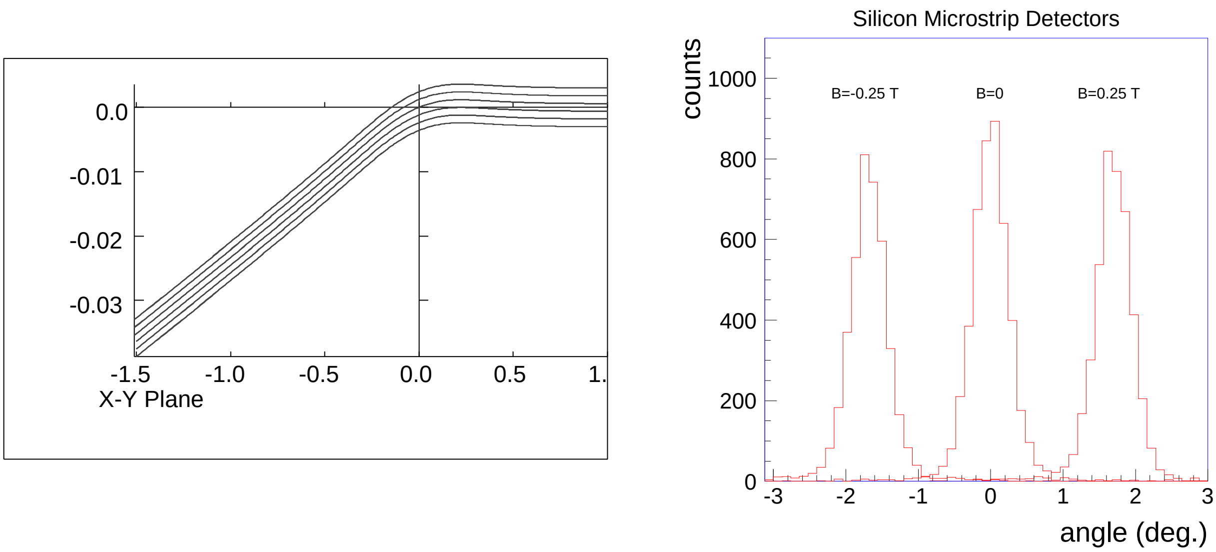

Figure 4.4: Deflection of the beam in the magnetic field. Left panel: trajectory of an ensemble of negative pions of 1 GeV for B=0.25 T. Values are in meters. The beam arrives parallel to the abscissa. Right panel: deflection of the beam, measured by the silicons for different fields.

4.3 Measurement of the Lorentz angle

In a magnetic field $\vec{B}$ with a component perpendicular to the electric field $\vec{E}$, the drifting ionization electrons move on straight trajectories at an angle Ψ_L to the electric field lines (see appendix B). The case $\vec{B} \perp \vec{E}$ is realized in our measurements. The angle Ψ_L between the drift velocity $\vec{v}_D$ and the drift field $\vec{E}_D$ is called Lorentz angle. The $\vec{v}_D$ component perpendicular to $\vec{E}_D$ spreads the arrival positions of the ionization along the pad row, resulting in a displacement on top of the effect of the angle of incidence of the primary particle, as demonstrated in the left panel of Fig. 4.5. In the angle reconstruction, Ψ_L is superimposed on the real angle of incidence. This allows a direct measurement of Ψ_L, which has so far not been determined experimentally for the ALICE standard gas mixture Xe,CO_2(15%) (for a measurement for Xe,CO_2(20%) see [19]).

In the magnetic field measurements, the incident angle of the beam is not identical to the chamber tilt. As discussed in section 4.1, the beam trajectory is curved. In Fig. 4.5, we show in the left panel the situation for a straight track and in the right panel the (realistic) case with deflection. The negative pions are deflected into the same direction as the drifting electrons. Consequently, the real angle of incidence is given by the chamber tilt reduced by the beam deflection at the chamber position. By symmetry, the deflection angle in the DC (placed at the center of symmetry) is exactly half of the deflection angle measured by the SIMs.

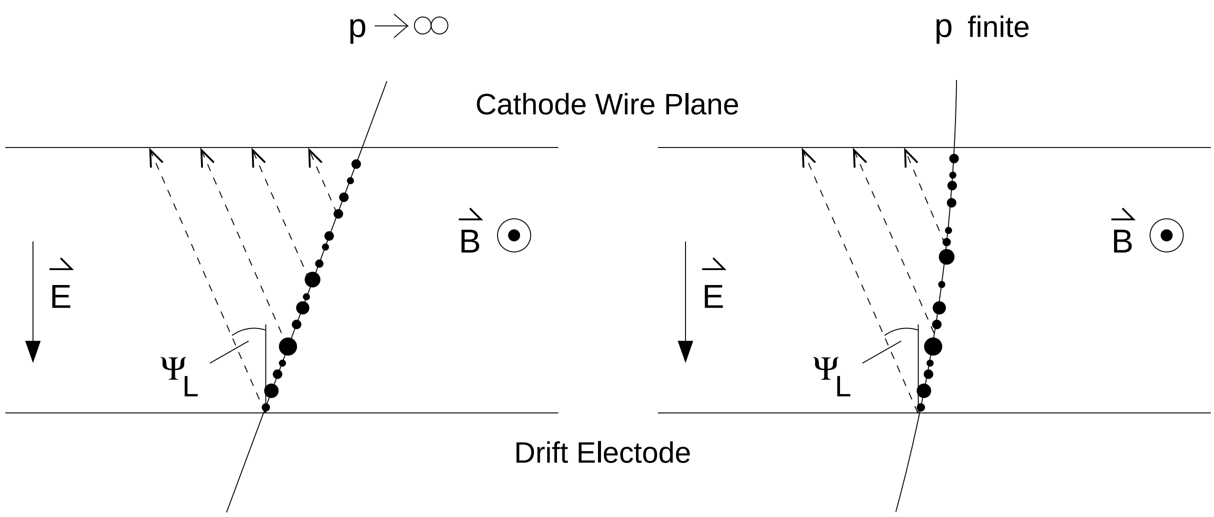

Figure 4.5: Drift path of electrons with magnetic field for a straight track (left panel) and a track curved under the influence of the magnetic field (right panel).

In Fig. 4.6 we show, for different values of the chamber tilt, the contributions to the Lorentz angle reconstruction. The drift field is 0.67 kV/cm. Under the particular circumstances during the B-field measurements, the tilt could not be determined accurately. We estimate the error to 1.5° The open squares mark the DC mean reconstructed angle at B=0, a measure of the chamber tilt (which is used instead of the 'mechanical' estimate of the chamber tilt, to avoid the large error of this measurement). The full triangles represent the beam deflection at chamber position. In the case B=0 (open triangles), the deflection is 0°. The errors on the silicon measurements represent the spread of the beam.

The full squares label the DC reconstructed angle for B=0.25 T. The difference to the B=0 case is striking. The errors on the measurements represent the uncertainty in assigning the drift time interval from the shape of the average pulse height as function of time. They reflect the systematic uncertainty about the limits of the drift time interval, both with respect to the passage from amplification peak to drift plateau and with respect to the end of the plateau. We estimate this error to Δt=0.1 μs. Using Eq. 3.6, we evaluate the resulting error on the reconstructed angle:

$$\Delta\Psi = \frac{\Delta t}{T} \cdot \Psi \tag{4.1}$$

$\Delta\Psi$ is proportional to Ψ, the error bars are small for small incidence and grow for higher tilt. To the DC reconstructed angle at B=0.25 T, we add the deflection of the beam. The results, labelled by full circles, correspond to the Lorentz angle, superimposed on the chamber tilt. The errors on the Lorentz angle are the quadratic mean of the errors on both silicon measurements (i.e. the square root of the sum of the squared errors) plus the systematical error on the DC measurements for B=0.25 T. We do not add errors of the DC measurements for B=0, since, for given drift field, the limits of the plateau in the cases B=0 and B=0.25 T are identical.

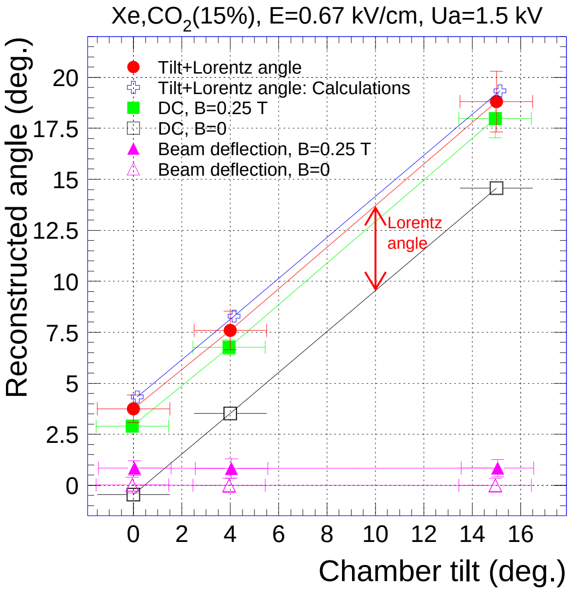

Figure 4.6: Construction of the Lorentz angle in a magnetic field of 0.25 T and a drift field of 0.67 kV/cm. The different contributions are explained in the text. The measured values of the Lorentz angle are compared to GARFIELD/MAGBOLTZ calculations.

The Lorentz angle measurements for different chamber positions agree well with each other. We compare them with the GARFIELD/MAGBOLTZ [15, 16] value. The measured Ψ_L=4.2° is smaller than the predicted value of 4.8°, but agrees well within the measurement errors.

For the case $\vec{E} \perp \vec{B}$, realized in our measurements, the Lorentz angle is a simple function of the cyclotron frequency ω=$\frac{e}{m}$·B and the mean time τ between two collisions (see appendix B):

$$\tan \Psi_L = \omega\tau$$

The microscopical quantity τ is connected to the mobility μ of the drifting electrons, μ=$\frac{e}{m} \cdot \tau$. Consequently, the Lorentz angle depends on the strength of the magnetic field as well as the drift field (via the field dependence of the mobility, demonstrated in Fig. 2.7). In Fig. 4.7, in the left panel, we present the Lorentz angle measured at E=0.67 kV/cm for values of B between $\pm$0.28 T. The results agree well with GARFIELD/MAGBOLTZ. We assume an error of 7% in B, as estimated in section 4.1. The errors on the angle are determined as described above. Measurements with different values of the magnetic field have only been performed at a high chamber tilt of 15° (the runs were originally not dedicated to the measurement of the Lorentz angle). In the DC measurements, the Lorentz angle is superimposed on the tilt. According to Eq. 4.1, the high angle results in large errors and leads to a significant increase of the error bars with increasing angle.

In the right panel of Fig. 4.7, we present results for the Lorentz angle as function of the drift field, for B=0.25 T. Experimental results and predictions are in reasonable agreement, although the measured Lorentz angle seems to be systematically smaller than the calculations. The discrepancy increases with higher field. This can be explained by the imperfect isolation of the amplification region against the drift region, which has been discussed in section 2.4. With increasing drift voltage, the amplification region extends more and more into the drift region. Using the $\langle \mathrm{PH} \rangle$ distribution, we overestimate the drift time interval, not taking the effective truncation of the drift region into account. At the same time, we also overestimate the drift length, using the geometrical depth of the drift region. Calculating the angle according to Eq. 3.6, we should ideally employ a shorter drift time T in the numerator and also a smaller drift length D in the denominator. An overestimate of the drift length D results in a linear relative underestimate of the angle. As we have seen in section 3.2, variations of the drift time interval affect the the reconstructed angle very little, and the variation of the numerator of Eq. 3.6 can not compensate for the overestimate of the denominator. Consequently, at high drift field, the Lorentz angle is systematically smaller than calculated with GARFIELD/MAGBOLTZ.

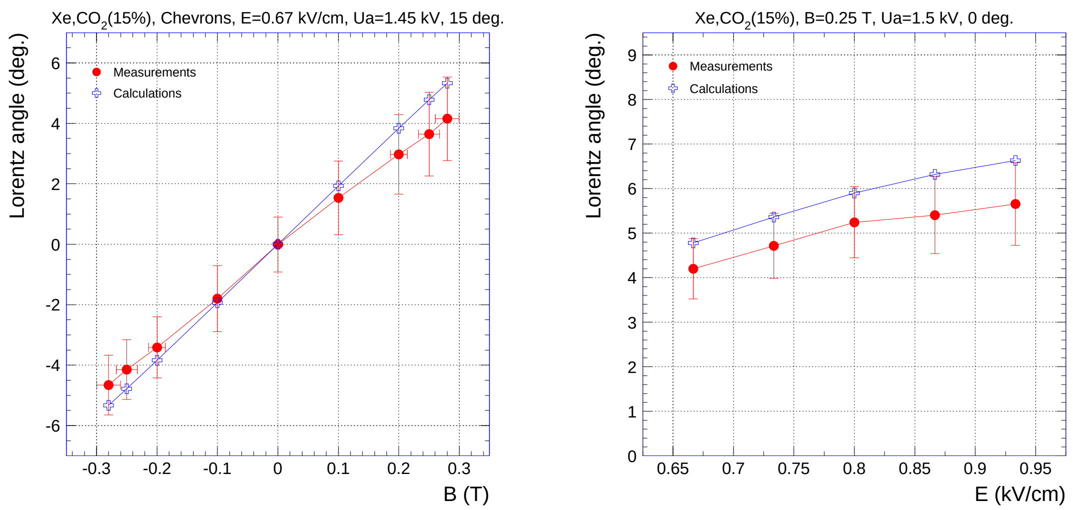

Figure 4.7: Measured Lorentz angle for different values of the magnetic field (left panel) and of the drift field (right panel). The results are compared to GARFIELD/MAGBOLTZ calculations.

4.4 Position resolution

An important limitation on the position resolution performance of the drift chambers arises from δ-electrons. These are produced in quasi-elastic collisions of the incident beam particle with electrons from atoms of the detector gas. These 'knock-on' electrons have high energies in excess of a few keV [13], and consequently a long range in the detector gas. They are emitted at an angle with respect to the primary trajectory, distorting the position resolution.

A particle with charge q moving at velocity $\vec{v}$ in a magnetic field $\vec{B}$ is subject to the Lorentz force $\vec{F} = q \cdot \vec{v} \times \vec{B}$. In a homogeneous field, the trajectory of the particle is a helix, its projection onto a plane normal to $\vec{B}$ is circular. For a particle with unit charge $|q|$=e, the radius R of this circle is, in good approximation [17],

$$R = \frac{10}{3}\Big(\frac{Tm}{GeV/c}\Big)\,\frac{p_\perp}{B} \tag{4.2}$$

where $p_\perp$ denotes the momentum component perpendicular to $\vec{B}$. Since the B-field within the chamber volume is quasi homogeneous, we use this formula to evaluate R for a δ-electron of 10 keV in a 0.25 T field: the resulting radius R=1.3 mm is much smaller than the width of a readout pad, but much bigger than the point resolution. We recall the experimental setup and the chamber geometry: the magnetic field lines are vertical. The anode wires, defining the coordinate of the point measurements along the pads, run horizontally, perpendicular to the B-field lines. The most harmful δ-electrons, those emitted horizontally, have an important $p_\perp$ component. They curl up in the field. For this reason, we expect an improvement of the position resolution by the magnetic field.

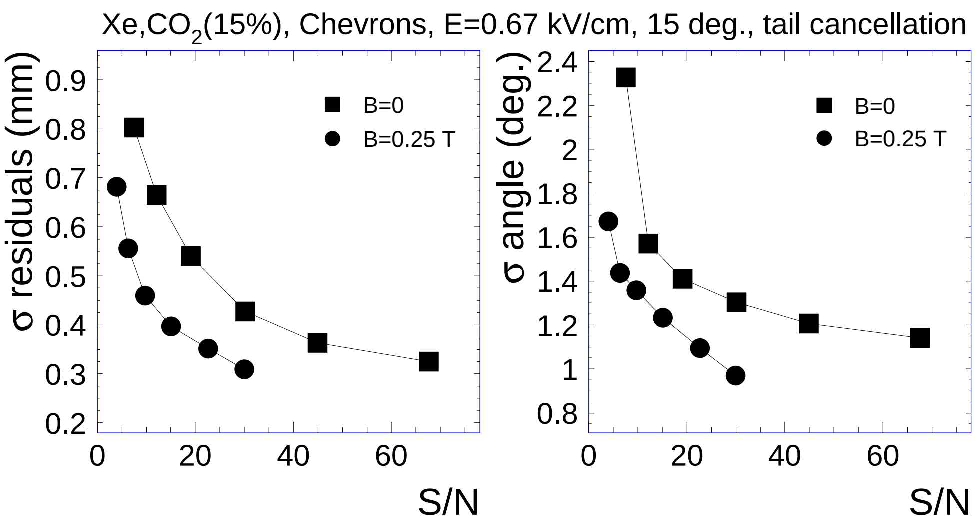

Figure 4.8: Position resolution (left panel) and angular resolution (right panel) as function of the signal-to-noise ratio in a magnetic field of B=0.25 T and for B=0. The chamber tilt is 15°.

In Fig. 4.8, we compare the resolution as function of the signal-to-noise ratio with and without magnetic field. The drift field was 0.67 kV/cm, a time bin width of 20 ns was used; tail cancellation is applied. In the case B=0, the DC reconstructs a mean angle of 14.7°, corresponding to the 15° chamber tilt. When the magnetic field is applied, the DC mean reconstructed angle is 18.0°, equal to the tilt plus the Lorentz angle, reduced by the beam deflection angle. In the magnetic field runs, the chambers suffered from high noise, in the order of 8 FADC channels, compared to 2 channels in the field free runs. The high noise reduces the signal-to-noise ratios in the B-field measurements. For given S/N, we find, as expected, a significant improvement of the position resolution by the magnetic field. At S/N=30, the point resolution (left panel) is 430 μm for B=0, it is 310 μm for B=0.25 T, which translates into an angular resolution of below 1° (right panel).

We already discussed the strong impact of the primary particle's incident angle on the position resolution. In Fig. 4.9, we compare the resolution achieved in the cases B=0.25 T and B=0 for a chamber tilt of 0°. At low incident angle, the ion tails are attenuated by the effect of gas gain saturation. As the spread of the ionization over the anode is small, subsequent avalanches are formed close to each other, and the field around the wire gets screened. The effect of ion tails is reduced, and the tail cancellation procedure does not result in an improvement of the resolution. The data taken at low incidence are relatively sparse, we only measured at low gain. To avoid the reduction of S/N by the tail cancellation algorithm, we present uncorrected results. We show point (left panel) and angular resolution (right panel) for S/N values up to $\sim$35. As expected from the discussion in section 3.3, the resolution achieved at low incidence is better than for the 15° tilt. Even at a S/N ratio as low as 16, we achieve in the B-field measurements a point resolution of 235 μm and an angular resolution of 0.7°. The improvement of the point resolution by the B-field is evident. In case of the angular resolution, the effect is less pronounced, due to the higher angle of incidence of 2.5° in the B-field measurements, compared to -0.4° for B=0. For B=0, an angular resolution of 0.5° for S/N=36 is reached.

In Fig. 4.10, we systematically compare the resolution with and without B-field as function of the reconstructed angle. Since the effect of the tail cancellation strongly depends on the angle of incidence and varies as function of the S/N ratio (see the discussion of Fig. 3.13 in section 3.3), we present a study of the uncorrected data. To compare similar S/N, we show B-field data taken at an anode voltage of U_A=1.55 kV and B=0 data at lower gain, U_A=1.45 kV. Nevertheless, there remains a difference in the S/N ratios, S/N$\approx$20 for B=0 and S/N$\approx$15 for B=0.25 T.

In the upper left panel, we present the position resolution. Without magnetic field, the reconstructed angle corresponds to the chamber tilt. For B=0.25 T, the curve is shifted to larger angles, since the chambers superimpose the Lorentz angle on the incidence. The improvement of the position resolution by the magnetic field is about 150 - 250 μm, depending on the angle. The angular resolution (upper right panel) also

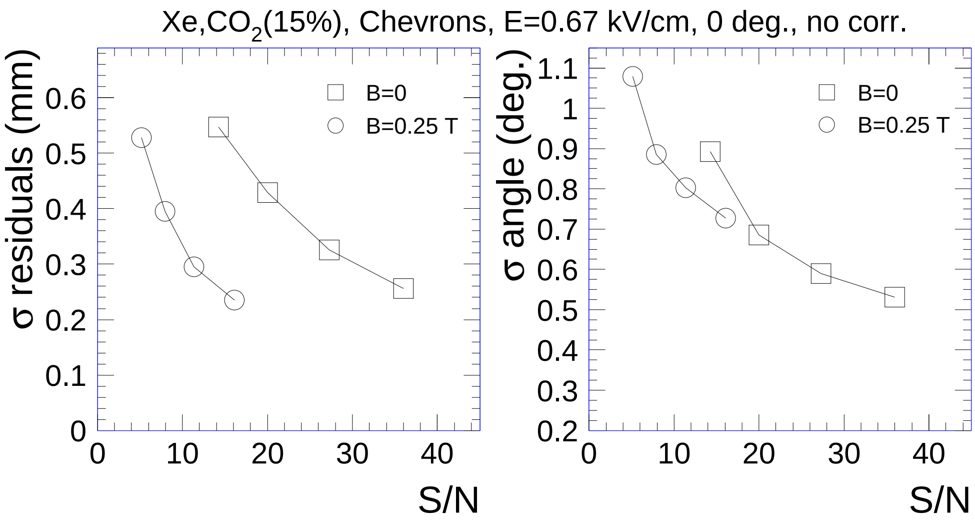

Figure 4.9: Position resolution as function of signal-to-noise ratio at 0° chamber tilt. No tail cancellation is applied. We compare the cases B=0 and B=0.25 T.

benefits from the magnetic field, but the effect is less pronounced. The reason is the higher S/N in the free field case. At low values of S/N, even small S/N variations lead to important changes of the resolution. The precise signal-to-noise ratios corresponding to each point in the upper panels are given in the lower left panel of Fig. 4.10. Each of the two distinct curves displays an evolution: the S/N increases with the chamber tilt, since the segment of the primary particle track within the chamber volume is longer at higher beam incident angle.

To correct the angular resolution for the effects of the S/N variations, we extrapolate each measured value of angular resolution presented in the upper right panel of Fig. 4.10 to the value for a common S/N of 15. For 0° and 15° incidence, we get the relative corrections to the angular resolution from S/N scans. For the B field case, at small angles the measured S/N is $\sim$10, and the correction to the value of S/N=15 corresponds to an improvement of the resolution. At large angles, the effect is small. For B=0, the correction from S/N$\approx$20 to S/N=15 leads to a degradation of the resolution. From the corrections at extreme incidence, we interpolate linearly to find the corrections for the 4° and 10° chamber tilt. The result is presented in the lower right panel of Fig. 4.10. After correction, the difference between the cases with and without magnetic field is much more pronounced. The figure clearly demonstrates the improvement due to the magnetic field.

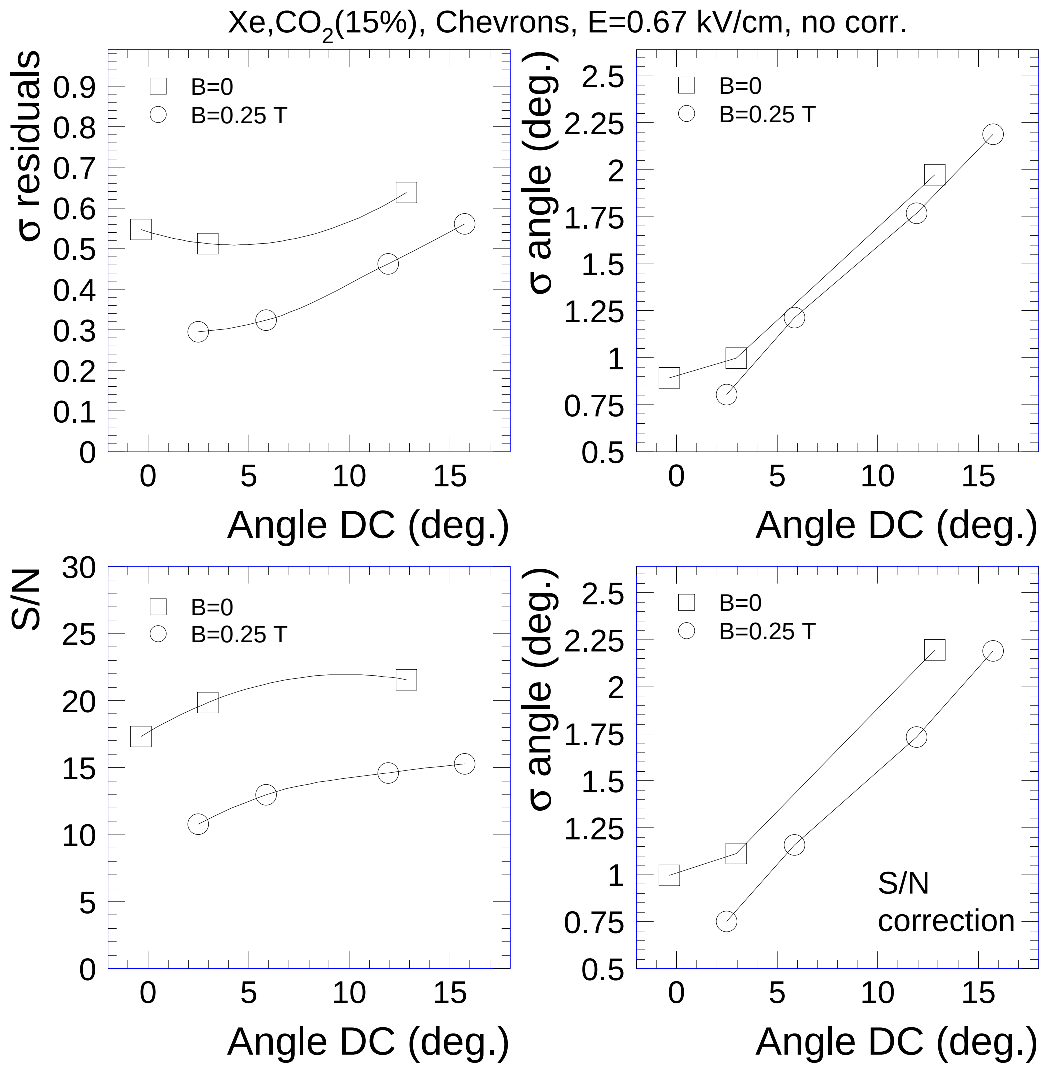

Figure 4.10: Position resolution as function of the reconstructed angle. Upper row: point (left panel) and angular resolution (right panel) versus DC reconstructed angle for B=0 and B=0.25 T. Lower row, left panel: S/N ratio for the cases shown above. Right panel: angular resolution, corrected to a common S/N ratio of S/N=15.

5 Lorentz angle measurements for a Ne,CO_2 mixture

In November 2001, we performed prototype tests at the pion beam facility at CERN PS. We carried out measurements in a magnetic field, operating two drift chambers in a dipole magnet. The original intention had been to perform position resolution studies with the rectangular pad prototypes in the B-field, using the ALICE TRD standard xenon based gas mixture. This was not possible: it turned out, that our stock of xenon suffered from SF_6 contamination, which affected the detector performance drastically. Therefore we decided to operate the chambers with neon. Neon based drift gas mixtures are widely used, e.g. in the NA49 Vertex TPCs (Ne,CO_2(9%)) and the CERES TPC (Ne,CO_2(20%)) experiments. We present measurements of the Lorentz angle in Ne,CO_2(13%). The odd 87:13 ratio of the compontents of the mixture was caused by a miscalibrated flowmeter, as was realized after the runs. Still, our results provided useful information for the calibration of the CERES TPC.

5.1 Setup

The experimental setup of the prototype tests with neon is shown in Fig. 5.1. In the large dipole magnet, currents up to 285 A created fields up to 0.4 T. We operated the detectors between the upper and lower poles of the magnet, in a gap of dimensions 0.3 m$\times$1.1 m$\times$1.0 m (height$\times$width$\times$depth).

We tested two DC with rectangular pads, identical in geometry and pad shape to the rectangular pads chamber described in chapter 3. Both silicon detectors were placed before the drift chambers. Due to the limited space and to difficulties shielding the detector for the high field, it was not possible to use the Pb-glass calorimeter for the magnetic field runs.

Beam momenta reached at the PS were higher compared to the SIS. We present results for a pion beam of 4 GeV/c. The natural electron content at this momentum is $\sim$7%. Without the information of the Pb-glass detector, we use a one-dimensional cut on the signal from the Cherenkov detector to exclude electrons from our analysis.

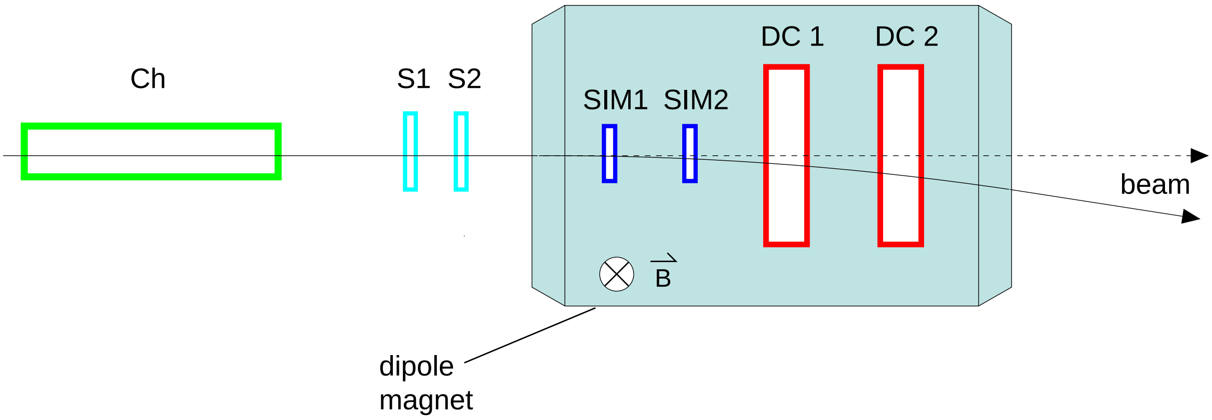

Figure 5.1: Setup of the measurements in the magnetic field at CERN. The drift chambers are placed in a dipole magnet. The deflection of the negative pion beam is sketched.

5.2 Measurements of the magnetic field

In Fig. 5.2 we present field measurements, performed with a Hall probe, at different positions in the dipole magnet and for different current densities. As usual, the beam axis coincides with the z-axis; the horizontal coordinate perpendicular to the beam is labelled ’x’, the vertical coordinate is labelled ’y’. The field lines in the dipole are vertical, so the measured component is B_y.

The upper panels show the field for different points on the beam axis; z=0 and z=100 cm correspond to the rims of the iron poles, B values for z$<$0 and z$>$100 cm measure the stray field, up- and downstream with respect to the magnet. We measured at x=0, in the middle between the left and right edges of the ground plate and at a height y=16 cm, corresponding to the central pad row in the drift chamber. The agreement with the nominal field of 140 mT (upper left panel) and 70 mT (upper right panel) is perfect over a wide range. The field becomes gradually smaller at the beginning and the end of the the poles, for z$<$20 cm and z$>$80 cm. The two silicon detectors were placed at z$\approx$7cm and z$\approx$33 cm, the chambers at z$\approx$52 cm and z$\approx$74 cm. The deviation from the nominal field is most important for the first silicon detector, where it is well below 10%. We assume that effects at the boundary do not affect our measurements, and consider the magnetic field uniform along the beam axis.

In the lower row of Fig. 5.2, we present measurements at z=70 cm, in the gap. For a nominal field of 140 mT, we measured along the horizontal x axis, at a height y=16.5 cm (left panel). In the interval between $\pm$10 cm, corresponding to more than 3 times the width of a pad row, the field variations are less than 3%. The variations along the vertical (right panel), midway between the left and right edges of the poles are equally negligible. The field strength rises in proximity of the poles, but the difference to the nominal field does not exceed 3%.

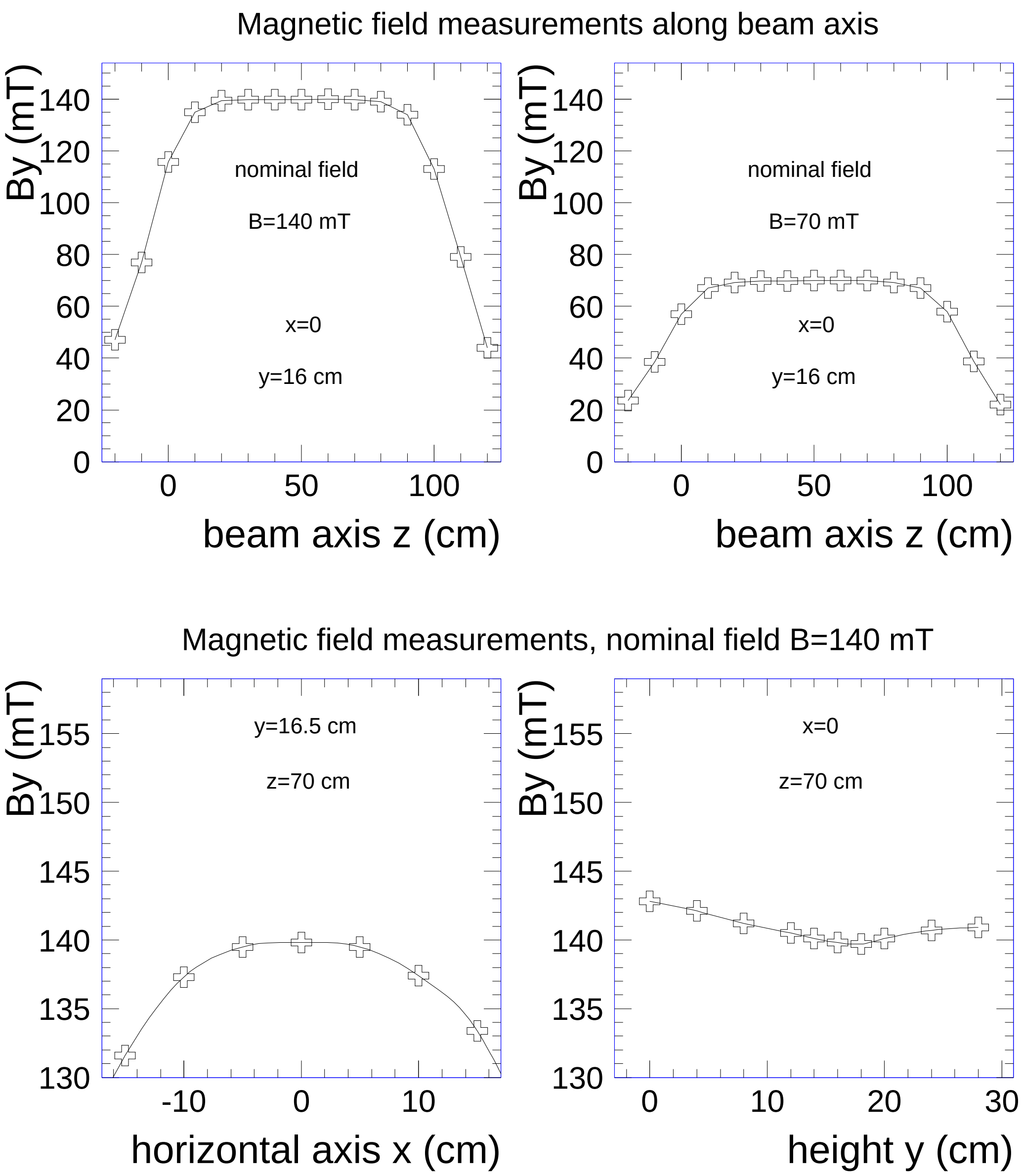

Figure 5.2: Magnetic field of the dipole magnet. Upper row: measurements along the beam axis for different values of the nominal field. Lower row: measurements along the horizontal and vertical.

5.3 Deconvolution of the signal

As in the case of xenon, we apply a tail cancellation to remove correlations between adjacent time bins and to cope with their negative effects on the position resolution of the detector. In Fig. 5.3 we compare the situation without deconvolution (upper panels) to results after the tail cancellation (center panels). On the left, we show the

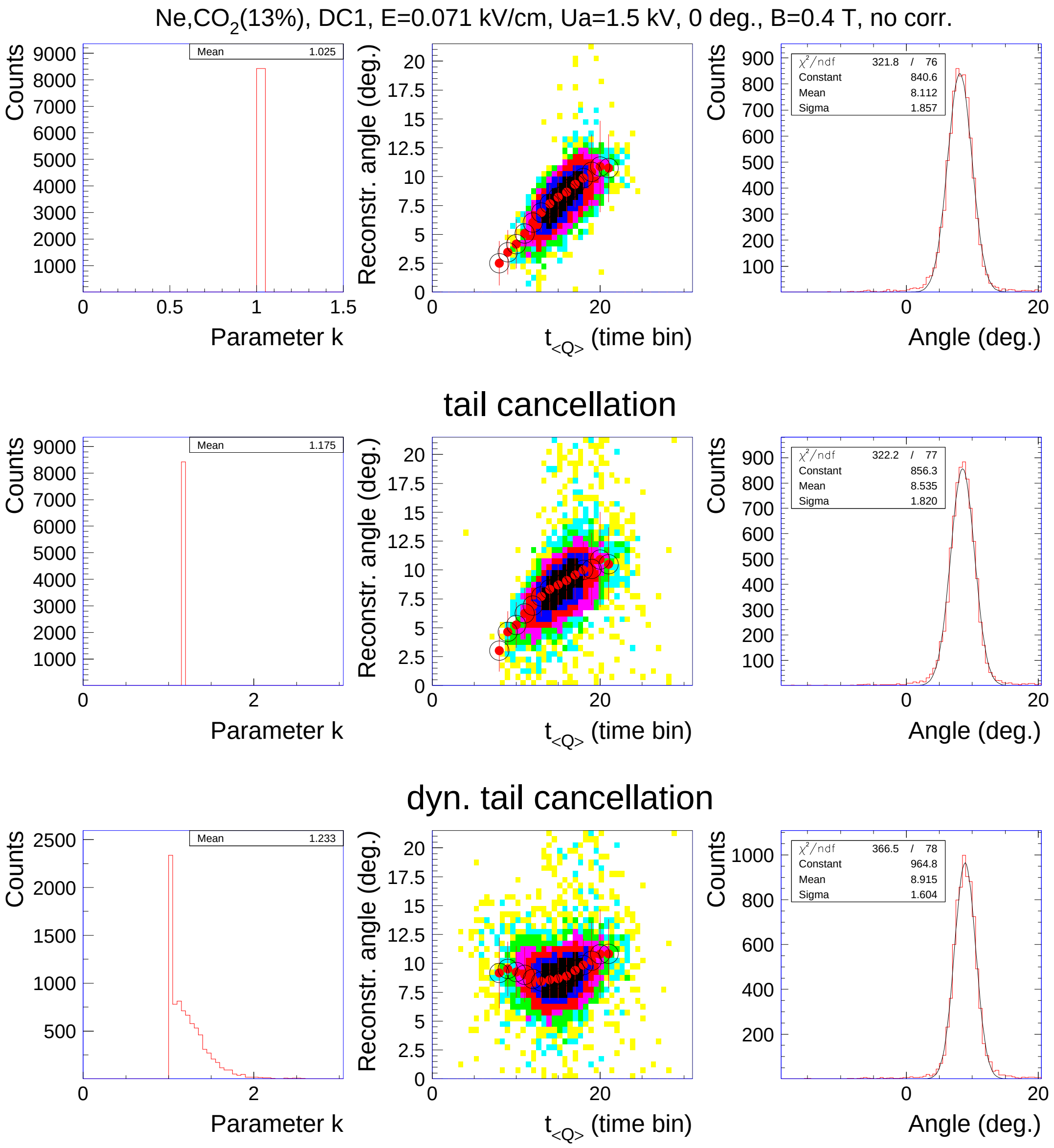

Figure 5.3: Effect of different methods of deconvolution. We show the values of the deconvolution parameter k (left panel), the correlation between reconstructed angle and the center of gravity of the signal $t_{\langle Q \rangle}$ (center panel) and the angle distribution (right panel). Results without tail cancellation (upper row), with tail cancellation with constant k (center row), and with a dynamic tail cancellation (lower row) are compared.

parameter k. The case without correction is equivalent to a unity transfer function (eq. 3.8), i.e. $f(s) \equiv$1, corresponding to k=1. The small deviation from 1 indicated in the histogramm is due to the finite bin size. For the tail cancellation, we choose the constant deconvolution parameters k=1.18 and τ=1.8 μs, optimizing the angular resolution. The choice of parameters is different to the xenon case, a result of the different ion mobility of neon. In the center panels, we show the correlation between the reconstructed angle and the center of gravity of the signal, $t_{\langle Q\rangle}$. In contrast to the case of xenon, the tail cancellation is not effective. For reasons not yet fully understood, the correlation remains to a high degree, and the improvement of the angular resolution (right panels) by the deconvolution is small.

Better results are achieved with a 'dynamic' tail cancellation. In this procedure, we vary the tail cancellation parameter k for each event. k is determined as function of $t_{\langle Q\rangle}$, according to the equation

$$\frac{1}{k} = \frac{1}{k_0} + \left(2\,\frac{t_{\langle Q\rangle}}{T} - 1\right)\Delta k \tag{5.1}$$

k_0 is the constant parameter of the original tail cancellation The inverse of k is varied linearly around k_0^{-1}, depending on the position of $t_{\langle Q\rangle}$ within the drift time interval T. A new parameter, Δk, is introduced. It governs the strength of the variations: in case Δk=0, the dynamic tail cancellation reduces to the original method with $k(t_{\langle Q\rangle}) \equiv k_0$. If for an event the charge deposit within the drift time happens to be exactly balanced, i.e. $t_{\langle Q\rangle} = T/2$, the variable k also takes the value k_0. For smaller $t_{\langle Q\rangle}$, corresponding to a more important influence of the tails, $k(t_{\langle Q\rangle})$ takes bigger values, which leads to a stronger reduction of the signal by the cancellation procedure.

The effect of the dynamic tail cancellation is demonstrated in the lower row of Fig. 5.3. In the left panel we show the distribution of the parameter k for all events, achieved with k_0=1.18, Δk=1.2. In case the value of k given by eq. 5.1 lies in the unphysical interval k <1 (resulting in an increase of the pulse height by the deconvolution), we set k=1. Adapting k to each event, we significantly reduce the correlation between the time bins, as is shown in the center panel. A major improvement of the angular resolution (right panel) is achieved.

5.4 Measurement of the Lorentz angle

Our tests of drift chamber prototypes in the dipole magnet allowed to determine the Lorentz angle of Ne,CO2(13%) for different magnetic and electric fields. The principle of the Lorentz angle determination is the same as described in section 4.3: in the angle reconstruction with the drift chambers, the Lorentz angle is superimposed on the real incidence, which is given by the chamber tilt and the beam deflection. The main difference is the position of the silicon detectors: in the CERN magnetic field runs these were placed upstream the DC, in the magnetic field. We have to extrapolate from the deflection measured in the silicons to the deflection angle at the chambers' position. The situation is sketched in Fig. 5.4. Since the field of the dipole is uniform, the beam trajectory is circular. Using eq. 4.2, we calculate the radius of this circle for a π^- particle. For a pion of 4 GeV/c momentum in a field of B=0.4 T we find R=33 m. The beam hits the two silicons, placed at a distance d from each other, and one drift chamber, at a distance l. The silicon detectors measure two points of the trajectory, x1 and x2. These two position measurements, however, are not sufficient to reconstruct the circle. To extrapolate the trajectory to the chambers, we have to use the calculated radius R. With this information, we can derive the incident angle β at the DC position as function of the angle θ measured by the two silicons.

The beam hits the silicons at the points (x_1, z_1) and (x_2, z_2). We write the coordinates in terms of the beam incident angle at these points and the radius R:

$$x_1 = R \cdot \cos\,\alpha_1 \quad x_2 = R \cdot \cos\,\alpha_2 \tag{5.2}$$

$$z_1 = R \cdot \sin\,\alpha_1 \quad z_2 = R \cdot \sin\,\alpha_2 \tag{5.3}$$

z_1 and z_2 are related via

$$d = z_2 - z_1 \tag{5.4}$$

The angle θ measured by the silicons is given by the difference of the x coordinates

$$\tan\,\theta = \frac{\Delta x}{d} = \frac{x_1 - x_2}{d} = \frac{R}{d}(\cos\,\alpha_1 - \cos\,\alpha_2) \tag{5.5}$$

$$= \frac{R}{d}\left(\sqrt{1-\sin^2\alpha_1} - \sqrt{1-\sin^2\alpha_2}\,\right) \tag{5.6}$$

We relate the sin terms via eq. 5.4 and eq. 5.3

$$\sin\,\alpha_1 = \sin\,\alpha_2 - \frac{d}{R} \tag{5.7}$$

Injecting 5.7 into 5.6, we get

$$\tan\,\theta = \frac{R}{d}\left(\sqrt{1-(\sin\,\alpha_2 - \frac{d}{R})^2} - \sqrt{1-\sin^2\alpha_2}\,\right)$$

Since the quadratic terms in this equation are small, we can expand the square root, according to $(1-x)^{\frac{1}{2}} \approx 1 - \frac{1}{2}x$:

$$\tan\,\theta = \frac{R}{d}\Big(1 - \frac{1}{2}(\sin\,\alpha_2 - \frac{d}{R})^2 - (1 - \frac{1}{2}\sin^2\alpha_2)\Big)$$

$$= \sin\,\alpha_2 - \frac{d}{2R}$$

$$\sin\,\alpha_2 = \tan\,\theta + \frac{d}{2R} \tag{5.8}$$

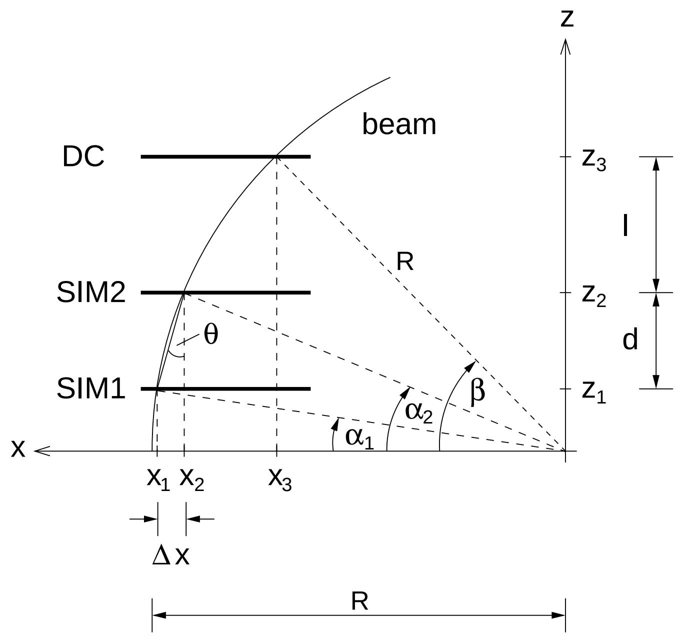

Figure 5.4: Schema of the circular beam trajectory, traversing the silicon detectors (SIM) and a drift chamber. The angle β is determined as function of θ, as described in the text.

We emphasize, that the term $\frac{d}{2R} \approx \frac{0.3\ m}{30\ m}$= 0.01 in eq. 5.8 can not be omitted, since we are dealing with small angles of the order of 1°, or ∼0.01 rad. To derive β, the angle of incidence at the drift chamber, we write

$$\begin{aligned} z_3 &= R \cdot \sin\beta = z_2 + l \\ \sin\beta &= \frac{z_2}{R} + \frac{l}{R} = \sin\alpha_2 + \frac{l}{R} \\ &= \tan\theta + \frac{d}{2R} + \frac{l}{R} \end{aligned}$$

For small angles, we finally get

$$\beta_{1,2} = \theta + \frac{d + 2l_{1,2}}{2R} \tag{5.9}$$

where $l_{1,2}$ denotes the distance between SIM2 and the first or second drift chamber, respectively. As explained, we cannot avoid using the calculated quantity R to determine the beam deflection. R is sensitive to inhomogeneities of the magnetic field, which lead to a deviation of the local radius of curvature of the trajectory from the value R determined for homogeneous field. We estimate the variation of β as function of R, according to eq. 5.9:

$$\frac{\Delta\beta}{\beta} \le \frac{\Delta R}{R}$$

(the equality sign holds for θ=0). Since θ and the R dependent term of eq. 5.9 are of similar magnitude, we find, that a 10% variation $\Delta R/R$ only leads to changes of $\Delta\beta/\beta$=5% and below. The small field inhomogenities have no practical impact on the estimate of the beam trajectory.

In Fig. 5.5, we present the results of the Lorentz angle measurements. For each chamber, we add the calculated beam deflection to the reconstructed angle and substract the chamber tilt. The measurements were performed at normal incidence, but, due to imperfect mounting, with residual angles of -0.9° for DC1, 1.4° for DC2, measured in the B=0 runs. We apply the dynamical tail cancellation. We show the results as function of the magnetic field, including measurements at negative polarity, for electric fields of ~0.3 kV/cm (left panel) and ~0.6 kV/cm (right panel). The errors of the measurement are due to the drift time estimate and the spread of the beam and are determined in the same way as in case of the xenon gas mixture. The results of both chambers and for both polarities are in excellent agreement. For low values of the drift field, the agreement with the GARFIELD/MAGBOLTZ [15, 16] calculations is very good. For higher electric field it is still resonably good, but the measured results are smaller than predicted. The discrepancy seems to be systematic and is more important in case of higher field.

In Fig. 5.6 we plot the measured Lorentz angle as function of the drift field, for different values of the magnetic field from 0.1 T to 0.4 T. We observe a systematical discrepancy between measurements and calculations at high drift field, similar to the case of xenon. The effect was discussed in section 4.3. Still, the overall agreement between our measurements and the predictions is reasonable. The results from both chambers are consistent.

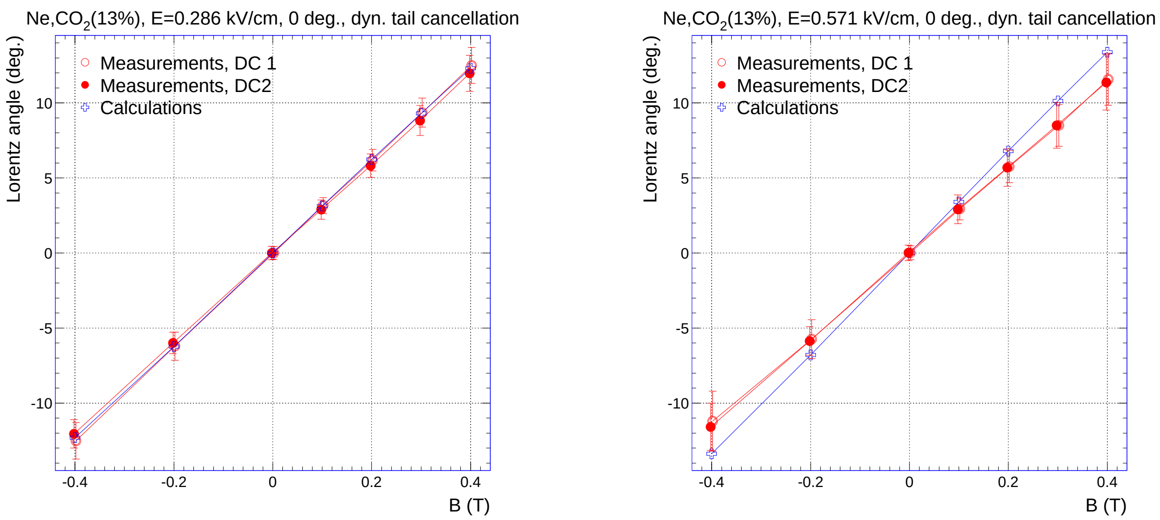

Figure 5.5: Lorentz angle as function of the magnetic field, including measurements at negative polarity, for given drift field.

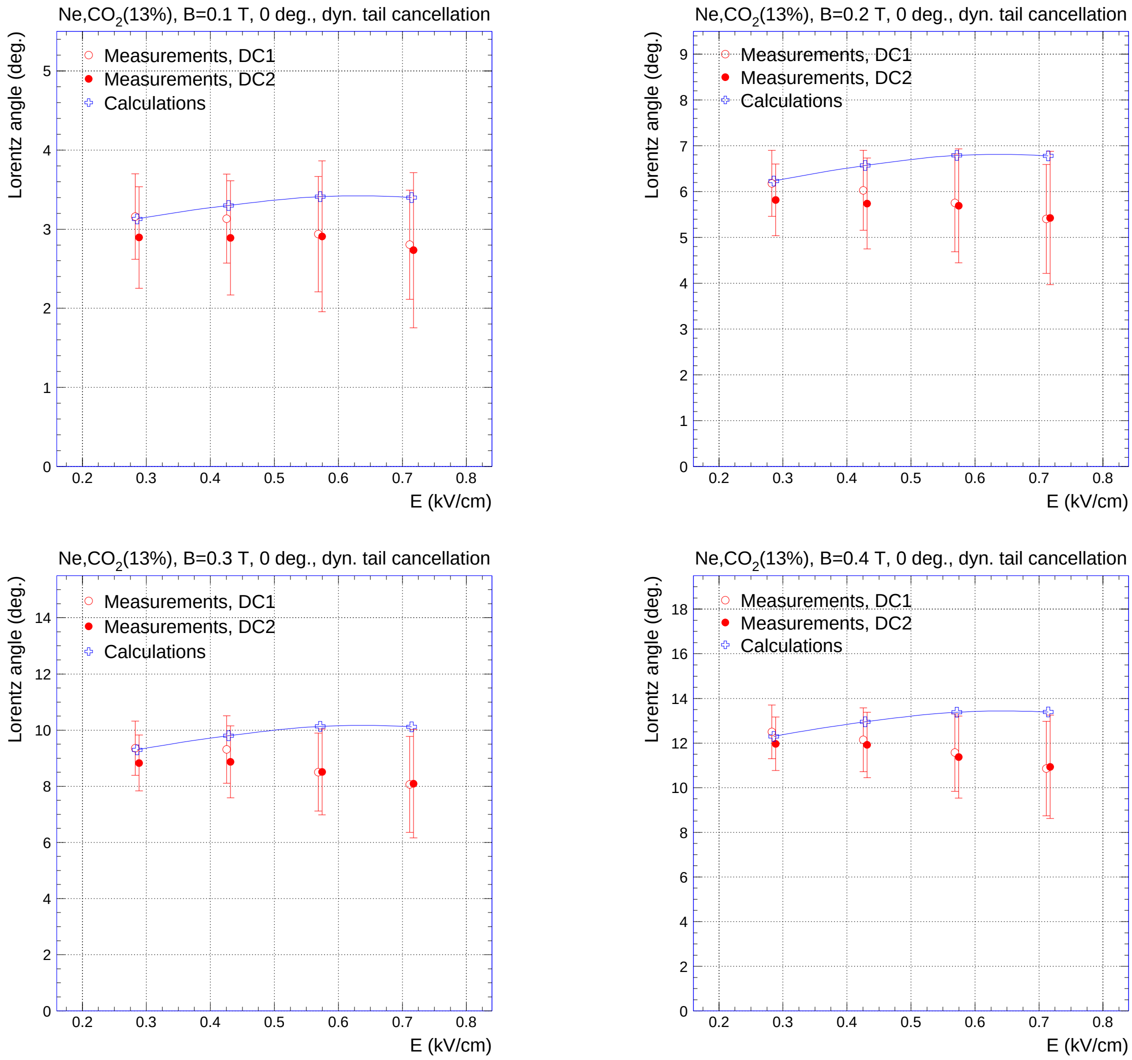

Figure 5.6: Lorentz angle as function of the electric field, for different values of the magnetic field.

Conclusions

We discussed various aspects of the position reconstruction with ALICE TRD prototypes. We demonstrated the important role of the signal-to-noise ratio for the position resolution of the detector. In the development of the TRD electronics, special effort is spent to optimize the gain of the preamplifier and to minimize detector noise. In the ALICE TRD readout chip, an online deconvolution will be performed by a digital filter, to cope with the influence of the xenon ion tails. We simulated the deconvolution by an offline tail cancellation and demonstrated its benefit for the position resolution.

The present TRD design specifies cathode pads of rectangular shape. We could show that, in terms of position resolution, this pad flavour is equivalent to the commonly used chevron type pads. Generally, rectangular pads display stronger nonlinearities of the pad response than chevrons (non-linearity is defined as the variation of the difference between the true and the reconstructed position as function of the position across the pad), but the effect is compensated by the smaller pad width (compare [20]). With regard to the choice ot the FADC sampling frequency, which in the final detector will be smaller than in the prototype tests, we also demonstrated, that the influence of the time bin width on the resolution is negligible.

We carried out studies of the position resolution in a magnetic field. At a signal-to-noise ration of 30-40, anticipated as operational point of the TRD, the drift chambers achieve a point resolution better than 300 μm and an angular resolution better than 1°. Given this performance, a momentum resolution of the final detector of $\delta p/p = 2.5\% \oplus 0.4\%\, p$ can be expected (with an estimate of the effect of multiple scattering as given in [2]). For an electron of 4 GeV/c, this translates into a momentum resolution better than 3%.

For the first time, the Lorentz angle for the ALICE TRD gas mixture was determined experimentally. The knowledge of this quantity is essential for the TRD trigger. Our results agree with the theoretical predictions.

The first prototypes of realistic size are under construction and will be tested in summer 2002. The construction of the TRD is going to start in 2003.

A Methods of deconvolution

The signal measured by the cathode pads is mainly induced by the motion of ions created in the avalanche around the anode wire. Since the massive ions move slowly compared to the PA sampling time, the signal exhibits a long tail. Convoluted with the response of the preamplifier/shaper, the ion tails give rise to a strong correlation between subsequent time bins. To reduce the effect, we apply a 'tail cancellation' algorithm, substracting the signal tail as function of time. The benefit of the deconvolution for the position resolution of the drift chambers is demonstrated in chapter 3. We describe the original approach [18], the correction of the signal at the level of the analog electronics by a pole/zero network. In the ALICE TRD readout chain, a digital filter will be employed.

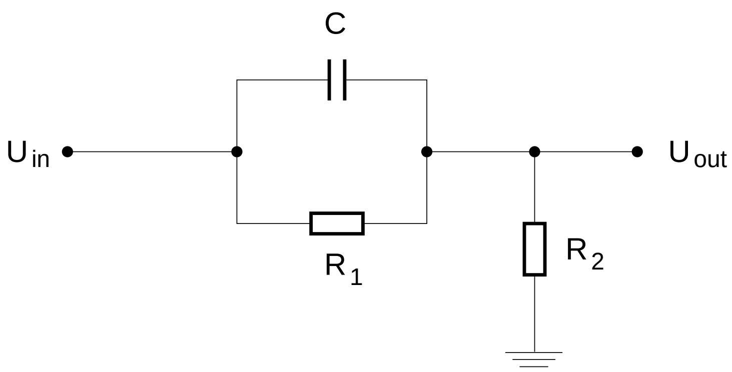

Figure A.1: Pole/zero network used for tail cancellation [18].

The offline deconvolution performs the signal processing of an R-C-network, presented in Fig. A.1. We derive the output as function of the applied signal. From Kirchhoff's voltage law we find the voltage U_{CR} at the R-C branch as function of the input voltage U_{in} and the output U_{out}

$$\begin{aligned} U_{in} &= U_{CR} + R_2 \cdot I \\ U_{out} &= R_2 \cdot I \qquad \text{(A.1)} \\ U_{CR} &= U_{in} - U_{out} \qquad \text{(A.2)} \end{aligned}$$

where I denotes the current through R_2.
From the charge of the condensator, $Q_C = C \cdot U_{CR}$, we find the related current

$$I_C = \dot{Q}_C = C \cdot \dot{U}_{CR}$$

whereas the current through R_1 is simply given by

$$I_{R_1} = \frac{U_{CR}}{R_1}$$

We apply Kirchhoff's current law to write I as the sum of the currents through R_1 and C:

$$\begin{aligned} I &= I_{R_1} + I_C \\ I &= \frac{U_{CR}}{R_1} + C \cdot \dot{U}_{CR} \end{aligned} \tag{A.3}$$

Injecting I from A.1 in the lhs of eq. A.3 and eliminating U$_{CR}$ using eq. A.2 we get

$$\dot{U}_{in} + \frac{1}{R_1 \cdot C} \cdot U_{in} = \dot{U}_{out} + (\frac{1}{R1 \cdot C} + \frac{1}{R_2 \cdot C}) \cdot U_{out}$$

Introducing $T = R_1 \cdot C$ and $k = \frac{R_1+R_2}{R_2}$, the differential equation of the circuit becomes:

$$\dot{U}_{in} + \frac{1}{T} \cdot U_{in} = \dot{U}_{out} + \frac{k}{T} \cdot U_{out} \tag{A.4}$$

We transform this differential equation to an algebraic equation in Fourier (or Laplace) space. The Fourier transformed signal is

$$\bar{U}(\omega) = \int_{-\infty}^{\infty} U(t) e^{-i\omega t} \mathrm{d}t$$

We also transform $\dot{U}(t)$:

$$\begin{aligned} \int_{-\infty}^{\infty} \dot{U}(t) e^{-i\omega t} \mathrm{d}t &= [U(t) e^{-i\omega t}]_{-\infty}^{\infty} - i\omega \int_{-\infty}^{\infty} U(t) e^{-i\omega t} \mathrm{d}t \\ &= -i\omega \cdot \bar{U}(\omega) \end{aligned}$$

respecting the boundary conditions for input and output, $U(-\infty) = U(\infty) = 0$.
We integrate eq. A.4 and solve for $\bar{U}_{out}$:

$$\bar{U}_{out} = \frac{\frac{1}{T} - i\omega}{\frac{k}{T} - i\omega} \bar{U}_{in} \tag{A.5}$$

One possible method of numerical deconvolution is to apply eq. A.5 with appropriately chosen constants k and T to the Fast Fourier Transform (FFT) of the signal. The resulting $\bar{U}_{out}(\omega)$ is transformed back via inverse FFT to get $U_{out}(t)$.
This method is numerically elaborate and time consuming. Therefore, we choose a different approach which turns out to be equally effective in terms of the position resolution.
Starting from eq. A.4, we use an approximate expression for the derivative:

$$\dot{U}(t) \rightarrow \frac{U(t) - U(t - \Delta t)}{\Delta t} \tag{A.6}$$

In our case, Δt is the time interval between 2 samples of the FADC. We write u_{i-1} and u_i, v_{i-1} and v_i for two subsequent samples of in- and output respectively, to get the discrete form of eq. A.4):

$$\frac{u_i - u_{i-1}}{\Delta t} + \frac{1}{T} \cdot u_i = \frac{v_i - v_{i-1}}{\Delta t} + \frac{k}{T} \cdot v_i$$

We solve for the output signal

$$v_i = \frac{1}{1 + k \cdot \frac{\Delta t}{T}} \cdot v_{i-1} + \frac{1 + \frac{\Delta t}{T}}{1 + k \cdot \frac{\Delta t}{T}} \cdot u_i - \frac{1}{1 + k \cdot \frac{\Delta t}{T}} \cdot u_{i-1}$$

and substitute $\kappa = \frac{1}{k}$ and $\tau = \frac{T}{\Delta t}$ to get, after some algebra

$$v_i = \frac{\kappa \cdot u_i + \kappa\tau \cdot (u_i - u_{i-1}) + \kappa\tau \cdot v_{i-1}}{1 + \kappa\tau} \tag{A.7}$$

This equation defines an numerical iteration. Starting with the signal vector $\vec{u}$, subsequent application of eq. A.7, using in each step the result $\vec{v}$ as new input, converges to the exact solution of the differential equation (the self consistent solution $\vec{v}$ = $\vec{u}$ of eq. A.7). The practical implementation of the offline tail cancellation employed for the position studies performs only one single step of the iteration, using effective constants κ and τ which optimize the angular resolution.
This constraint obviously restricts the accuracy of the deconvolution, but the resulting limitations on the performance are tolerable. A more fundamental limit of the method is the accuracy of the discretisation of the differentials according to eq. A.6. A finer sampling of the signal, corresponding to a smaller Δt, improves the performance of the tail cancellation. On the level of the Fourier transformed differential equation, there is an equivalent restriction by the Nyquist theorem.

B Drift of electrons in gases

Particles with charge q and velocity $\vec{v}$ are subject to the Coulomb force $q\vec{E}$ in the electric field $\vec{E}$ and the Lorentz force $q\vec{v} \times \vec{B}$ in the magnetic field $\vec{B}$. If the particle moves in a gas filled volume, collisions with the gas atoms give rise to a stochastic, time-dependent force $m\vec{A}(t)$. The equation of motion for a drifting electron is [21]:

$$m\dot{\vec{v}} = -e(\vec{E} + \vec{v} \times \vec{B}) + m\vec{A}(t) \tag{B.1}$$

where m and $-e$ are the electron mass and charge, respectively. Since we are interested in the drift of the electron at constant drift velocity $\vec{v}_D$=$\langle\vec{v}\rangle$, the time average of the lhs of eq. B.1 must vanish. Hence, the stochastic deceleration $\vec{A}$ compensates, on average, the translatoric motion:

$$\vec{A}(t) = -\frac{\vec{v}_D}{\tau} \tag{B.2}$$

where τ is the mean time between two collisions. The time average of eq. B.2 then becomes

$$\dot{\vec{v}}_D = -e\vec{E}/m + \vec{v}_D \times e\vec{B}/m - \vec{v}_D/\tau \tag{B.3}$$

and, since $\dot{\vec{v}}_D = 0$ for constant $\vec{E}$

$$\vec{v}_D/\tau - e\vec{B}/m \times \vec{v}_D = -e\vec{E}/m$$

Rewriting this as a matrix equation and inverting the matrix, one obtains [17]

$$\vec{v}_D = (\frac{-\mu}{1 + (\omega\tau)^2})(\vec{E} + \frac{\vec{E} \times \vec{B}}{B}\omega\tau + \frac{(\vec{E} \cdot \vec{B}) \cdot \vec{B}}{B^2}\omega^2\tau^2)$$

The macroscopic moblity μ and the cyclotron frequency ω are given by

$$\mu = (\frac{e}{m})\,\tau, \qquad \omega = (\frac{e}{m})\,B \tag{B.4}$$

In presence of a magnetic field perpendicular to the electric field ($\vec{B} \perp \vec{E}$), as is the case in our measurements, the drift velocity has a component $\vec{v}_{D\perp}$ in direction of $\vec{E} \times \vec{B}$:

$$\vec{v}_{D\perp} = \mu E \frac{\omega\tau}{1 + (\omega\tau)^2}$$

The component $\vec{v}_{D\,\|}$ parallel to $\vec{E}$ is

$$\vec{v}_{D\,\|} = -\mu E \frac{1}{1 + (\omega\tau)^2}$$

From the two components we get the magnitude of the drift velocity v_D=$\|\vec{v}_D\|$:

$$v_D = \mu E \frac{1}{\sqrt{1 + (\omega\tau)^2}} \tag{B.5}$$

The angle between $\vec{v}_D$ and $\vec{E}$, the Lorentz angle, is

$$tan\Psi_L = \omega\tau \tag{B.6}$$

It is remarkable, that the Lorentz angle is determined by just two parameters ω and τ, where only τ reflects the complexity involved in the electron drift process. Using eqs. B.4 and B.5 and assuming that τ is independent of B, we can rewrite eq. B.6 in the following form [22]:

$$tan\ \Psi_L = (\frac{B}{E})\, v_D^0$$

where $v_D^0 = v_D\ (B = 0) = v_D\ (\omega = 0)$.

Bibliography

[1] ALICE Collaboration, Technical Proposal, CERN/LHCC/95-71.

[2] ALICE Collaboration, Transition Radiation Detector, Technical Design Report, CERN/LHCC 2001-021, http://www-aix.gsi.de/ alice/trdtdr/index.html

[3] E.V.Shuryak, Phys.Lett. **B78**(1978) 150.

[4] V.L.Ginzburg and I.M.Frank, Zh.Eskp.Teor.Fiz. **16**(1946) 15.

[5] Particle Physics Booklet, July 2000

[6] T.Matsui and H.Satz, Phys.Lett. **B178**(1986) 416.

[7] H.Satz, hep-ph/0007069.

[8] M.C.Abreu et al. (NA 50), Phys.Lett. **B 450**(1999) 456.

[9] P.Braun-Munzinger and J.Stachel, Phys.Lett. **B490**(2000) 196.

[10] R.S.Simon, Prog.Part.Nucl.Phys. **42**(1999) 247.

[11] H.G.Essel and N.Kurz, IEEE Trans.Nucl.Sci **47**(2000) 337.

[12] RIO2 8062, Creative Electronic Systems S.A., http://www.ces.ch

[13] R.K.Bock and A.Vasilescu, The Particle Detector Briefbook, Springer Verlag, 1998.

[14] A.Steigerwald, diploma thesis, January 1997, http://www-hades.gsi.de/gsi/docs/AchimSteigerwald_Diplom.ps.gz

[15] R.Veenhof, Nucl.Inst.Meth. **A419**(1998) 726, http://consult.cern.ch/writeup/garfield/

[16] S.Biaggi, Nucl. Inst. Meth. **A421**(1999) 234.

[17] W.Blum and L.Rolandi, Particle Detection with Drift Chambers, Springer-Verlag, 1994.

[18] R.A.Boie et al., Nucl.Inst.Meth. **192**(1982) 365.

[19] U.Becker et al., Nucl.Inst.Meth. **A421** (1999) 54-59
Gas R&D Home Page, http://cyclotron.mit.edu/drift

[20] ALICE Collaboration, Time Projection Chamber, Technical Design Report, CERN/LHCC 2001-001, http://alice.web.cern.ch/Alice/TDR/

[21] K.Kleinknecht, Detektoren für Teilchenstrahlung, Teubner, 1984.

[22] K.Hoshina et al., Nucl.Inst.Meth. **A479**(2002), 278.

Acknowledgements

I want to express my gratitude to many people who have been important to me during my time at GSI.

In first place, I want to thank Prof. Peter Braun-Munzinger, who gave me the unique opportunity to work in ALICE TRD and guided my first steps into heavy ion physics. I am deeply indebted to my supervisor and teacher Anton Andronic. I profited very much from his advice, his enthusiasm, his support and patience.

Many people contributed to this work: Reinhard Simon and Marco Gersabeck installed the Helmholtz coils at GSI. I profited very much from Marco's experience with the OPERA software. Marian Ivanov contributed the tail cancellation algorithm. Alexandro Castillo was not afraid of being ionized and polarized during the field measurements in the CERN magnet. With Dariusz Miskowiec and Ana Marin I had many inspiring discussions about the Lorentz angle measurements. I want to thank all the colleagues participating in the beam times at GSI and CERN and all collaborators from ALICE TRD.

I am graceful to the people who made my time at GSI such a nice one, in particular the people from CERES not mentioned above, Hiro Sako, Chilo Garabatos and Gunar Hering. I thank Jutta Reiß, Ingo Peter, Günther Siegert, Udo Meyer and Klaus-Dieter Groß for the pleasant atmosphere during my work for the scientific management.

I finally express my thankfulness to my parents for their encouragement and support, which allowed me to study physics. Without them, this work would not have been realized.

Erklärung zur Diplomarbeit gemäß $19 Abs. 6 DPO/AT

Hiermit versichere Ich, die vorliegende Diplomarbeit ohne Hilfe Dritter nur mit den angegebenen Quellen und Hilfsmitteln angefertigt zu haben. Alle Stellen, die aus den Quellen entnommen wurden, sind als solche kenntlich gemacht worden. Diese Arbeit hat in gleicher oder ähnlicher Form noch keiner Prüfungsbehörde vorgelegen.